AD_____

AWARD NUMBER: W81XWH-07-1-0591

TITLE: Non-Invasive Monitoring of Intra-Abdominal Bleeding Rate Using Electrical Impedance Tomography

PRINCIPAL INVESTIGATOR: Rosalind Sadleir, Ph.D. and Edward A. Ross, M.D.

CONTRACTING ORGANIZATION: University of Florida
Gainesville, FL 32611

REPORT DATE: September 2009

TYPE OF REPORT: Final

PREPARED FOR: U.S. Army Medical Research and Materiel Command
Fort Detrick, Maryland 21702-5012

REPORT DOCUMENTATION PAGE

Form Approved
OMB No. 0704-0188

1. REPORT DATE	2. REPORT TYPE	3. DATES COVERED
1 September 2009	Final	3 Aug 2007 – 31 Aug 2009

4. TITLE AND SUBTITLE

Non-Invasive Monitoring of Intra-Abdominal Bleeding Rate Using Electrical Impedance Tomography

5a. CONTRACT NUMBER

5b. GRANT NUMBER
W81XWH-07-1-0591

5c. PROGRAM ELEMENT NUMBER

6. AUTHOR(S)

Rosalind Sadleir, Ph.D. and Edward A. Ross, M.D.

E-Mail: sadleir@ufl.edu

5d. PROJECT NUMBER

5e. TASK NUMBER

5f. WORK UNIT NUMBER

7. PERFORMING ORGANIZATION NAME(S) AND ADDRESS(ES)

University of Florida
Gainesville, FL 32611

8. PERFORMING ORGANIZATION REPORT NUMBER

9. SPONSORING / MONITORING AGENCY NAME(S) AND ADDRESS(ES)
U.S. Army Medical Research and Materiel Command
Fort Detrick, Maryland 21702-5012

10. SPONSOR/MONITOR'S ACRONYM(S)

11. SPONSOR/MONITOR'S REPORT NUMBER(S)

12. DISTRIBUTION / AVAILABILITY STATEMENT
Approved for Public Release; Distribution Unlimited

13. SUPPLEMENTARY NOTES

14. ABSTRACT

Electrical Impedance Tomography (EIT) may be useful in continuous non-invasive monitoring of suspected abdominal bleeding in battlefield casualties subsequent to blunt trauma. We are developing a novel EIT system involving an electrode array applied only to the anterior abdomen. We believe this will speed this method's path to practical use. Much of the work in the revised Statement of Work has been completed. A no cost extension was granted to complete this work due to equipment and approval problems delaying initiation of the clinical phase. We have successfully devised a method to translate data gathered from a novel eight-electrode array to quantity of blood-like anomaly. We have performed tests on volunteer subjects to determine the extent of breathing and motion artifacts on measurements. While breathing can have large effects, normal breathing does not obscure detection of ingested blood-like fluids. The EPack system has been reconstructed to improve its robustness. Two publications, three conference presentations, a PhD proposal and two related patents have been published or granted.

15. SUBJECT TERMS
Intraperitoneal hemorrhage, hemorrhage triage, electrical impedance tomography, Filtering, hemiarray

16. SECURITY CLASSIFICATION OF:			17. LIMITATION OF ABSTRACT	18. NUMBER OF PAGES	19a. NAME OF RESPONSIBLE PERSON
a. REPORT	b. ABSTRACT	c. THIS PAGE			USAMRMC
U	U	U	UU	61	19b. TELEPHONE NUMBER *(include area code)*

Standard Form 298 (Rev. 8-98)
Prescribed by ANSI Std. Z39.18

Table of Contents

Page

Introduction

Intra-abdominal bleeding is commonly associated with blunt trauma to the abdomen, occurring frequently as a consequence of detonations, falls and motor vehicle accidents. It is usual to diagnose intraperitoneal bleeding by the presence of clinical signs such as high pulse rate, low blood pressure and abdominal guarding or tenderness. However, in many patients, particularly those between 20 and 30 years of age, these signs may not appear until a life-threatening amount of blood has been lost. A method or device that can rapidly determine bleeding rate as well as total blood loss during monitoring is essential for rapid assessment of blunt trauma injury. Estimation of bleeding rate as well as total blood volume lost could be an important triage factor. In a field situation with limited personnel, or where there are mass casualties to be evaluated, it would be advantageous to use an automated method that is specific to the injury, simple to apply and requires little operator input or expertise. Existing imaging or diagnosis methods for intra-abdominal bleeding are either impractical for field use (MRI/CT), non-specific (pulse, blood pressure) operator dependent (ultrasound/DPL) or invasive (DPL) Thus, EIT is a potentially highly sensitive and useful technique for detecting and monitoring intra-abdominal bleeding. The aim of using EIT in this context is both to clearly identify seriously high rates of bleeding as well as total blood loss during monitoring, with the aim of avoiding unnecessary laparotomy, operator dependent or intensive procedures and significantly, to provide a method of triaging or monitoring multiple casualties. In this work, we have tested an electrically based method for detection of bleeding that uses an eight-electrode array applied to the anterior abdomen. We have used a peritoneal dialysis model to allow an examination of how normal body signals such as breathing and motion degrades detection of simulated bleeding and bleeding rate.

Body

Timeline

Initial distribution of funding for the two-year project was in August 2007, with original end date of 30 September 2009. In October 2007 USAMRAA reduced the funding duration to 30 September 2008 and a reduced statement of work was submitted and approved. Unfortunately, IRB approval of all USAMRAA-requested modifications to our protocol was not approved until March 19, 2008 and recruitment of subjects and performance of procedures was delayed. In addition, equipment problems resulted in our refabricating the board to make it more robust during clinical testing. A no cost extension of the one-year

project to 30 September 2009 was granted in August 2008. In the text below we have ***highlighted*** tasks in the grant statement of work, with relevant details following beneath.

Research Accomplishments

1. Perform belt evaluations on normal volunteers.

A Modify belt design and attachment; B Evaluate belt material longevity and connection integrity

We tested belt properties and found that belt shielding and contact worked well when used with electrode contact gel as intended. The initial tests were performed using individual carbon rubber electrodes, however, because the original belt (fixed) size was too large for the subjects tested. The belt size can easily be scaled by scaling the layout plan, but after having tested the two basic features (shielding and contact quality) we decided to delay testing until subjects of suitable sizes became available. Once we have determined that the belt works in-vivo and does not require any further modifications apart from sizing we will perform all tests using individual carbon rubber electrodes.

C Evaluate unit battery life and efficiency

Unit battery life was found to be acceptable for testing periods of about 1 hour. The Director of Clinical Engineering at Shands at the University of Florida, Craig Bakuzonis, advised us during safety testing of our device that we could use mains connected transformers to power the device during clinical testing and we will either use this approach or battery power depending on the testing time used. Most monitoring procedures will take around 1 hour, but when patients allow we may extend the number of peritoneal fluid exchanges and consequently monitoring time. We found that the EPack II consumed around 2W power.

Improvements in device performance and reliability

The system is shown in Figure 1 [From Tucker 2009b]. We improved the performance of the system greatly by implementing improved hardware and firmware design. Some aspects of these improvements are described below, and are the subject of a manuscript currently in preparation. Two components of the system, one partial component that determines electrode contact quality and another that comprises the system as a whole, are being patented separately. The electrode contact quality system, configured as a means to detect needle disconnection in hemodialysis, has recently

been awarded (May 12, 2009) US Patent 7,530,962. Another patent for the whole system is currently under examination.

Figure 1 Photograph of second generation EPack device, showing housing, Bluetooth antenna and eight electrode connections (left) and (right) device PCB.

Improvements in Aperture Time

The amount of time necessary to capture a complete set of boundary voltage measurements is defined as the aperture time. A short aperture is important to reduce blurring associated with physiological processes like breathing and blood flow. For a hemi-array system with n_E electrodes there are a total of n_E distinct current injections pairs. For each injection, (n_E - 3) voltage measurements are recorded so there are a total of $n_E(n_E - 3)$ voltage measurements per acquisition. For the EPack, $n_E = 8$, so there are 40 measurements in total. Each of these voltage measurements requires a sampling period $t_{sample} = \frac{n_C}{f_0}$. Therefore the minimum theoretical acquisition time is:

$$t_{a(\min)} = n_E(n_E - 3)\frac{n_C}{f_0}, \qquad [1]$$

where n_E is the number of electrodes, f_o is the frequency of the current injection and n_C is the number of current injection periods. EPack II averages over $n_C = 10$ periods, so the minimum theoretical aperture time is about 6.5 ms at 62.5 kHz.

Accounting for the delay caused by multiplexer settling, t_{mux}, the acquisition time is:

$$t_a = n_E(n_E - 3)\left(\frac{n_C}{f_0} + t_{mux}\right). \qquad [2]$$

EPack II allows t_{mux} = 1ms for multiplexer settling, so the expected acquisition time is 46.4 ms.

The aperture time is deterministic, and is measured using one of the DSP's internal timers. Figure 2 compares the aperture time in the two EPack generations. EPack II has a measured aperture time of 47ms.

The maximum frame rate measures how quickly the EPack system can record a measurement, calculate and display the reconstruction, and then continue to the next measurement. Frame rate is important because it measures how quickly information can be made available to clinicians. Frame rate includes the aperture time, the data transmission time, and the reconstruction time. The frame rate is nondeterministic and depends on the capabilities of the PC used. With a 2GHz Pentium IV processor, 1GB of RAM, and minimum background processes the frame rate is about 1.5 frames per second.

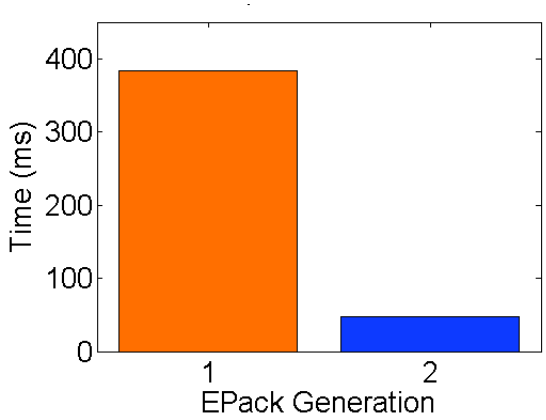

Figure 2 Comparison of aperture times in EPack1 and EPack2.0

A simple, resistive phantom was constructed from 16 identical resistors (100 Ω +/- 5%) arranged in a network with eight external nodes and one internal node. The resistor phantom is used to evaluate the EPack's basic performance independent of the electrode-skin interface. Using this phantom, we expect to achieve the best possible signal-to-noise ratio. EPack I and II were each used to make L = 1000 repeated measurements of the resistor phantom. Signal to noise is calculated using the method given by Cook et al[9]:

$$SNR = 10\log\frac{\sum_{l=1}^{L}\left(v(l)\right)^2}{\sum_{l=1}^{L}\left(v(l)-\bar{v}\right)^2} \qquad [3]$$

The results for each system are shown in Figure 3. The x-axis, labeled 'Measurement Index', represents each of the 40 transimpedance measurements. The measurement index variable corresponds to the 40 measurements that can be made with the 8 electrode array. The EPack II has a significantly better SNR than EPack I does.

.

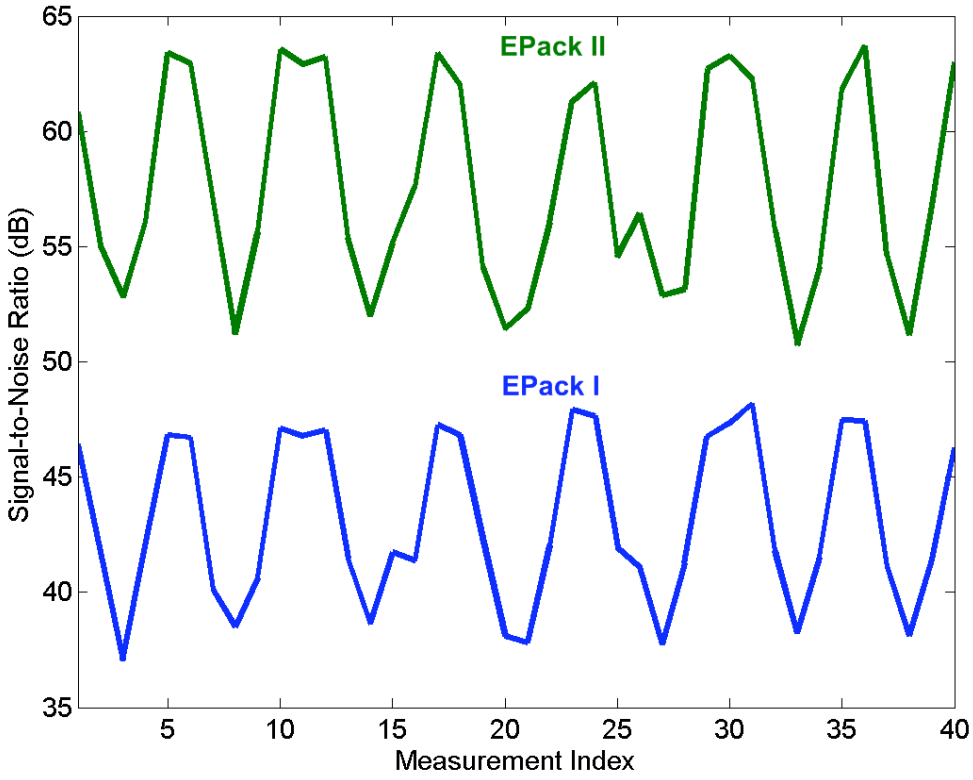

Figure 3 Comparison of SNR measured in a resistor phantom over the two EPack generations.

The SNR performance of the EPack is summarized in Figure 4. SNR is best in the resistor phantom, and is significantly worse in the saline phantom and *in-vivo* experimentation. Evidently, a large amount of noise is attributable to the presence of electrodes. The saline phantom has a noise level that closely approximates *in-vivo* noise.

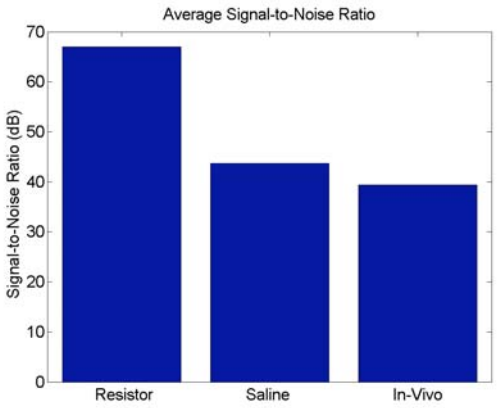

Figure 4 Comparison of SNR values measured in resistor phantom, saline tank and in-vivo.

Software development

A graphical user interface (GUI) to control the EPack was written using Visual C# 2008 (Microsoft, Redmond, VA). The software is used to initiate measurements, receive data, and display live reconstructions. The software is designed to be simple, fast and intuitive for first time users. A screenshot of the GUI is shown in Figure 5 below.

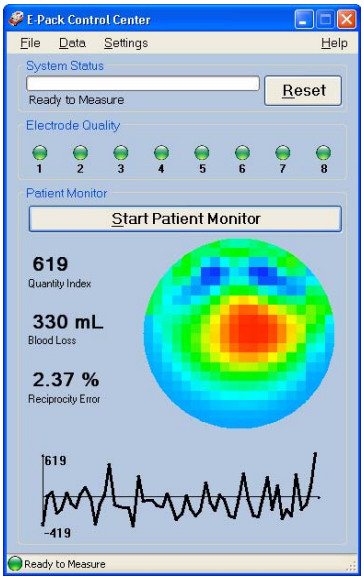

Figure 5 Screenshot of EPack 2.0 Control panel.

2. Determine appropriate in-vivo regularization and filtering parameters under controlled conditions

3. *Test reconstruction sensitivity under controlled conditions*[1]

Extensive tank testing was performed to determine the efficacy of an eight-electrode system in reconstructing and localizing conductive anomalies, and more critically, to determine the ability of the system to accurately quantify blood.

There must be some modification of the method used to determine quantity to correct for the spatial variance of the problem. This was achieved by determining the amount of spatial variance observed in QIs of 'ideal' anomalies (created using the sensitivity matrix) and dividing this out of real reconstructions. The procedure used is detailed in Sadleir et al. (2008). The correction was implemented by premultiplying the sensitivity matrix by these data and then performing inversion of the resulting matrix using truncated singular value decomposition (tSVD). The effect was to correct the reconstruction values but to avoid division by very small QI values by taking advantage of the truncation process to eliminate singular values by very small numbers. Before this correction was applied, we found that when we moved anomalies of different volumes (50 – 200 ml) at many different locations in the phantom we achieved QI values that had only a small amount of variance (an uncertainty in volume estimate of around 30 ml). This value is similar to the uncertainty target of the device.

Although these results were positive this test was only for anomalies moved within the electrode plane and using long electrodes that were extended the entire height of the phantom to create an approximately two-dimensional field pattern. Therefore we also tested the system using smaller electrodes and with anomalies moved in three different planes being either in (PL1); one half electrode length away from (PL2); or one full electrode length away from (PL3) the electrode plane. The uncertainty found was much greater in this study. On average the conversion constant (factor relating anomaly volume to QI) decreased as anomalies were moved in planes further away from the electrodes as found in earlier work[7]. Volume uncertainties in the PL1 case were found to be about 38 ml. However, after application of the correction described above, uncertainties in the two-dimensional case were reduced to about 15 ml and those in the three dimensional case were reduced to about 30 ml. Thus, after application of the correction method even

[1] This text is paraphrased from the annual report on this project for the period to 30 September 2008.

uncertainties in three-dimensional cases were close to the overall system target.

More recent testing [Oh et al. 2009] has resulted in an overall improvement in performance of hemiarray reconstructions by using different preconditioning matrices. Figure 6 below compares reconstructions of an anomaly moved in a phantom along the β direction when several different reconstruction methods were used. Details of the reconstruction methods may be found in Oh et al. (2009), attached to this document.

4. Determine sensitivity of image-derived measures to breathing and motion related artifacts. Implement compensation for periodic artifacts.

After phantom testing, the system was tested on volunteers (the investigators) to determine system reconstruction and quantification performance as a conductive fluid was introduced. This was done by performing a 'soup test'. In this test subjects fasted overnight, then had the eight electrode array attached. Baseline data were collected for a period of about 10 minutes. Following this period the subject was asked to breathe with extreme movement of the abdomen (extreme movement of the abdomen should greatly disrupt electrical field patterns and therefore the measurements collected. After this period another set of baseline data were collected and then soup at blood temperature and conductivity similar to blood was ingested by the subject as one or two 250 ml meals. The fluid was ingested through a straw in order to minimize any effects due to abdominal movement. We found that QI values during monitoring were stable enough for fluid ingestion to be detected. When subjects were asked to breathe shallowly (with minimal movement of the abdomen) we found a standard deviation in QI values of around 4.5 units. The change in QI observed on ingestion of 250 ml of soup was found to be around 0.046 units/ml. Therefore, the in-vivo noise floor was equivalent to around **100 ml** of orally administered fluid. We expected that the actual noise floor should be lower than this because the sensitivity of the electrode plane centered on the umbilicus to orally administered fluid should be low. For example, in phantom testing the sensitivity to blood-like conductivity anomalies placed one electrode length away from the center of the electrode plane was around half that found when the anomaly was placed at the center of the electrode plane. Other tests of the system on volunteers involved normal breathing and soup ingestion only. Other descriptions of results of oral fluid ingestion tests may be

found in the annual report for the year ending September 30, 2008.

5. Identify and initiate recruiting of male peritoneal dialysis subjects.

With the assistance of research staff at the satellite peritoneal dialysis clinic of Shands Hospital, we identified and recruited suitable subjects and performed study protocols during their monthly clinic visits.

6. Testing on peritoneal dialysis subjects

In the final phase of the project the device was tested on subjects undergoing peritoneal dialysis (PD). Typical results of the study protocol are shown in Figures 6 and 7 below.

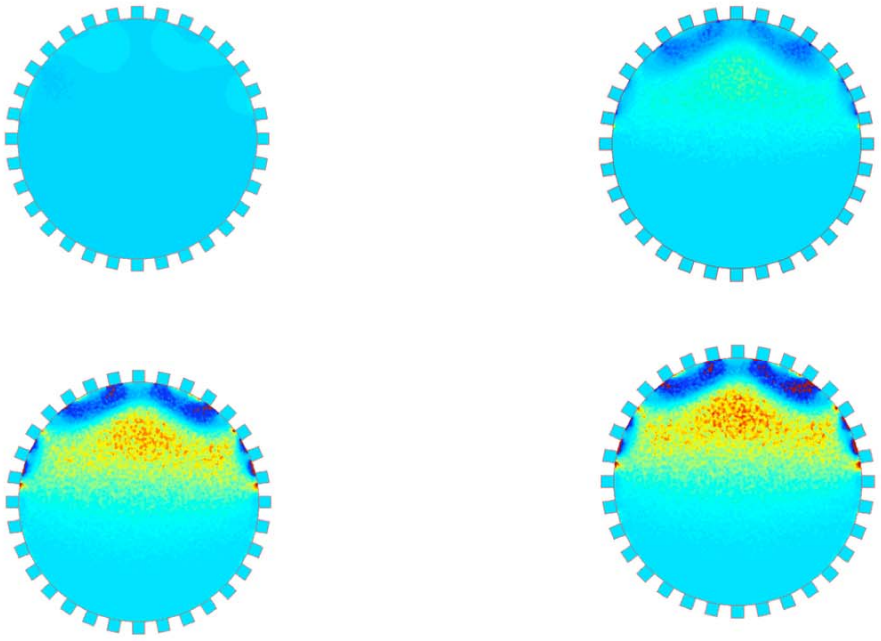

Figure 6 Hemiarray images before 0.3 min (top-left) during (top-right, 13.9 minutes), (bottom-left, 29 min) and after (bottom-right, 36.8 minutes) (bottom-right) dialysate infusion.

QI data shown in the top panel of Figure 7 were obtained by integration of unfiltered reconstructed data using a tSVD truncation index (k) of 12. Administered dialysate mass is shown

in g on the lower panel. QI values clearly correlate with amount of dialysate administered.

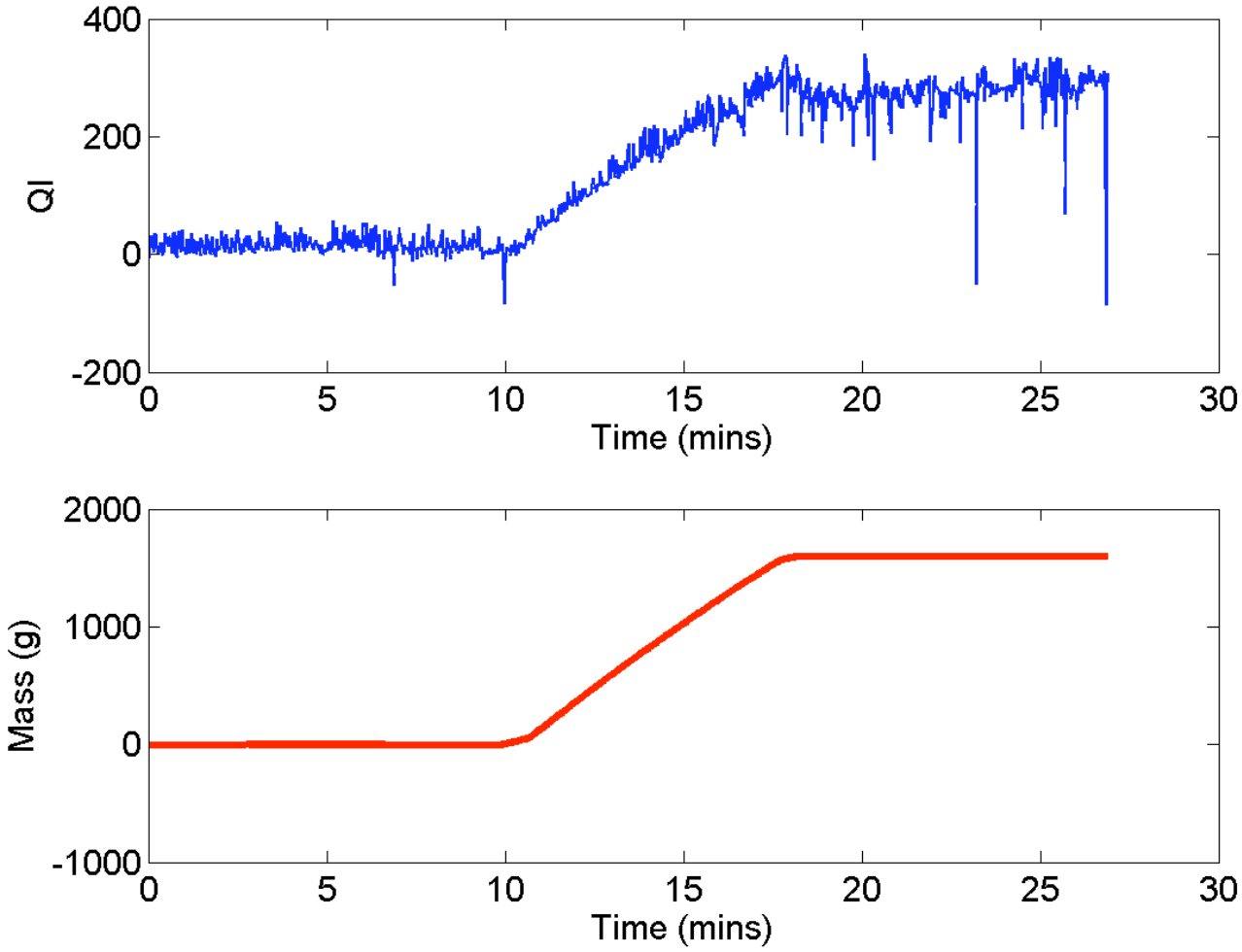

Figure 7. Example plot of (top) image data represented as post-processed quantity index (QI) and (below) amount of fluid administered.

a. Determine sensitivity to administration of peritoneal dialysate.

Average sensitivity was around **0.15 g^{-1}** in QI. Although insufficient subjects were monitored to do a full statistical analysis, it appeared that this sensitivity was independent of subject parameters such as mass, girth or height. We note that the sensitivity found in peritoneal dialysis subjects, where fluid was administered directly to the abdomen, was around 3 times the sensitivity of the method to orally administered fluid.

b. Determine sensitivity to normal breathing and movement-related changes

We estimated this factor by examining the quiescent noise, i.e. that present during normal breathing and movement, and not during fluid administration. The sensitivity to normal in-vivo processes can therefore be expressed in grams of free fluid by determining the ratio of the standard deviation in quiescent QI value to the fluid sensitivity. That is:

$$Sens_{noise} = \frac{std(0)}{a} \qquad [4]$$

where $Sens_{noise}$ is the sensitivity to normal in-vivo processes, expressed in g, $std(0)$ is the standard deviation of QI signals during these processes (and without fluid administration) and a is the factor connecting QI value with amount of fluid administered. In the subjects studied, $Sens_{noise}$ was between **60 and 70 g** of fluid, less than the minimum amount detectable using FAST ultrasound[8]. In some cases of extreme movement, for example a posture change, variation of QI was very large, but transient. In summary, we found that while the phantom sensitivity was around 40 ml without spatial filtering, inclusion of in-vivo artifacts resulted in an increase in detection floor to the equivalent of around **70 g** fluid.

c. Determine appropriate alarm levels

With this in mind, we have determined that an appropriate alarm level for intra-abdominal fluid is at the equivalent of **100 g** fluid. Although transients may increase the std(0) value, inclusion of a moving average filter with a width of 25 samples should result in these factors being removed.

7. Confirm Belt Design is appropriate on male subjects

Although we have performed many tests on volunteers and study subjects, nearly all have been made using commercially available carbon-rubber electrodes. It has not been possible to test the belt designed for the system because it is specific to larger girth subject sizes and we have not encountered subjects with large enough girths to enable proper testing.

Key Research Accomplishments

- Phantom, volunteer and subject Measurements have been made and analyzed as specified in the SOW.
- Parameters for detection of intraperitoneal bleeding have been determined.
- It was found that the in-vivo noise floor of the equivalent of around 60-70 g fluid administered to the abdomen was sufficiently low to enable unambiguous detection of significant bleeding.
- Instrumentation has been greatly improved in quality, with an improvement in SNR by around 20dB.

Reportable outcomes

- Two refereed journal publications have been published (a submitted paper referenced as Oh et al. 2008 was subsequently published as Oh et al. (2009))., two further journal publications are currently under preparation.
- Three conference publications or abstracts have been published or presented. In this year (2009) a presented at the 10th Conference on Biomedical Applications of Electrical Impedance Tomography held in Manchester, UK, June 11-15th, 2009 (Tucker et al. 2009).
- The project was the subject of a passed PhD thesis proposal (Tucker 2009b).

Students supported by this award

A. S. Tucker (PhD candidate, progressed to candidacy September 11, 2009) – has been involved in design and development of the EPack system, including power considerations and Bluetooth communication inclusion, as well as performing patient measurements.

Sungho Oh (PhD awarded May 2009) was involved in determining methods for regularization of hemiarray images, as well as evaluating methods for compensating for measurement changes caused by changes in boundary (abdomen) shape.

Conclusion

Our initial work using the EPack system with the eight-electrode hemiarray topology bore out our hypothesis that a novel eight-electrode system could successfully detect and identify blood-like anomaly volumes with uncertainties near to the 30 ml value sought. Tests of the system in-vivo to determine the method's robustness to breathing and motion artifact showed that these events did increase volume uncertainty but not significantly in the case of normal breathing.

In summary, we have been able to apply this method to detect and monitor conductive fluid in-vivo at the levels anticipated. Reducing the number of electrodes used has increased the overall volume uncertainty but taking this step has prepared the system for practical use in critical environments.

Our development steps beyond this project are to test the device in trauma environments, and to perform a prospective comparison of this method with FAST ultrasound and CT in blunt trauma cases presenting to the Level 1 Trauma Unit at the SHANDS/UF Medical Center.

References

1. “Imaging and quantification of anomaly volume using an eight electrode ‘hemiarray’ EIT reconstruction method”, R.J. Sadleir, S.U. Zhang, A.S. Tucker and Sungho Oh, *Physiological Measurement* 29 913-927 (2008) [Sadleir et al. 2008a]

2. “Normalization of Spatially-variant image reconstruction problem in Electrical Impedance Tomography using system blurring properties”, S. Oh, T. Te, A. S. Tucker and R.J. Sadleir, *Physiological Measurement* 30 275-289 (2009) [Oh et al. 2009]

3. “Method for detecting the disconnection of an extracorporeal device using a patient’s endogenous electrical voltages” US Patent Application 20070000847, filed 08/JUNE/2006, PCT/WO 2006/138359 published 28/DEC/2006. Ross, Sadleir, sponsors, Ross, Sadleir, inventors. [Ross, Sadleir 2006]

4. “Use of an eight-electrode hemiarray EIT electrode configuration for in-vivo fluid quantification”, R.J. Sadleir, A. S. Tucker, Sungho Oh and Te Tang, Proceedings EIT Conference 2008, Dartmouth College, Hanover, NH, 16-18 June, pp. 118-121, 2008 [Sadleir et al. 2008b]

5. “Portable eight-electrode EIT system for detection and quantification of abdominal hemorrhage”, R. J. Sadleir, A. S. Tucker, Sungho Oh and Te Tang, Proceedings EIT Conference 2008, Dartmouth College, Hanover, NH, 16-18 June, pp. 150-154, 2008 [Tucker et al. 2008]

6. “Internal Bleeding Detection Apparatus” PCT WO 2007/070978 filed 28/DEC/2006 published 28/JUN/2007 EIT Pty Ltd, sponsor, Sadleir, Duncan, inventors. [Sadleir, Duncan 2006]

7. “Quantification of blood volume by Electrical Impedance Tomography using a tissue equivalent phantom”, R.J. Sadleir, R.A. Fox, Physiol. Meas. 19, 501-516 (1998) [Sadleir, Fox 1998].

8. B. B. Goldberg, H. R. Clearfield, G. A. Goodman, and J. O. Morales, "Ultrasonic determination of ascites,"*Arch Intern Med*, vol. 131, no. 2, pp. 217-220, February 1973.

9. R. D. Cook, G. J. Saulnier, D. G. Gisser, J. C. Goble, J. C. Newell, and D. Isaacson, "Act3: a high-speed, high-precision electrical impedance tomograph," *Biomedical Engineering, IEEE Transactions on*, vol. 41, no. 8, pp. 713-722, 1994.

10. “Preliminary Results from the E-Pack2: a Portable EIT System Optimized for Detecting Hemoperitoneum”, A. S. Tucker, R. J. Sadleir, Tang Te, Proceedings EIT Conference 2009, Manchester

University, Manchester, England, June 12-15, 2009

Bibliography (Publications Resulting from this Project)

1. “Imaging and quantification of anomaly volume using an eight electrode ‘hemiarray’ EIT reconstruction method”, R.J. Sadleir, S.U. Zhang, A.S. Tucker and Sungho Oh, *Physiological Measurement* 29 913-927 (2008) [Sadleir et al. 2008a]
2. “Normalization of Spatially-variant image reconstruction problem in Electrical Impedance Tomography using system blurring properties”, S. Oh, T. Te, A. S. Tucker and R.J. Sadleir, *Physiological Measurement* 30 275-289 (2009) [Oh et al. 2009]
3. “Method for detecting the disconnection of an extracorporeal device using a patient’s endogenous electrical voltages” US Patent Application 20070000847, filed 08/JUNE/2006, PCT/WO 2006/138359 published 28/DEC/2006. Ross, Sadleir, sponsors, Ross, Sadleir, inventors. [Ross, Sadleir 2006]
4. “Use of an eight-electrode hemiarray EIT electrode configuration for in-vivo fluid quantification”, R.J. Sadleir, A. S. Tucker, Sungho Oh and Te Tang, Proceedings EIT Conference 2008, Dartmouth College, Hanover, NH, 16-18 June, pp. 118-121, 2008 [Sadleir et al. 2008b]
5. “Portable eight-electrode EIT system for detection and quantification of abdominal hemorrhage”, R. J. Sadleir, A. S. Tucker, Sungho Oh and Te Tang, Proceedings EIT Conference 2008, Dartmouth College, Hanover, NH, 16-18 June, pp. 150-154, 2008 [Tucker et al. 2008]
6. “Internal Bleeding Detection Apparatus” PCT WO 2007/070978 filed 28/DEC/2006 published 28/JUN/2007 EIT Pty Ltd, sponsor, Sadleir, Duncan, inventors. [Sadleir, Duncan 2006]
7. “Preliminary Results from the E-Pack2: a Portable EIT System Optimized for Detecting Hemoperitoneum”, A. S. Tucker, R. J. Sadleir, Tang Te, Proceedings EIT Conference 2009, Manchester University, Manchester, England, June 12-15, 2009

Appendices

1. Sadleir et al. 2008
2. Oh et al. 2009
3. Sadleir et al 2008a
4. Sadleir et al. 2008b
5. Tucker et al. 2009.
6. Epack User Guide

IOP PUBLISHING PHYSIOLOGICAL MEASUREMENT

Physiol. Meas. **29** (2008) 913–927 doi:10.1088/0967-3334/29/8/005

Imaging and quantification of anomaly volume using an eight-electrode 'hemiarray' EIT reconstruction method

R J Sadleir, S U Zhang, A S Tucker and Sungho Oh

J Crayton Pruitt Department of Biomedical Engineering, University of Florida, Box 116131, Gainesville, FL, USA

E-mail: sadleir@ufl.edu

Received 20 February 2008, accepted for publication 28 May 2008
Published 4 July 2008
Online at stacks.iop.org/PM/29/913

Abstract

Electrical impedance tomography (EIT) is particularly well-suited to applications where its portability, rapid acquisition speed and sensitivity give it a practical advantage over other monitoring or imaging systems. An EIT system's patient interface can potentially be adapted to match the target environment, and thereby increase its utility. It may thus be appropriate to use different electrode positions from those conventionally used in EIT in these cases. One application that may require this is the use of EIT on emergency medicine patients; in particular those who have suffered blunt abdominal trauma. In patients who have suffered major trauma, it is desirable to minimize the risk of spinal cord injury by avoiding lifting them. To adapt EIT to this requirement, we devised and evaluated a new electrode topology (the 'hemiarray') which comprises a set of eight electrodes placed only on the subject's anterior surface. Images were obtained using a two-dimensional sensitivity matrix and weighted singular value decomposition reconstruction. The hemiarray method's ability to quantify bleeding was evaluated by comparing its performance with conventional 2D reconstruction methods using data gathered from a saline phantom. We found that without applying corrections to reconstructed images it was possible to estimate blood volume in a two-dimensional hemiarray case with an uncertainty of around 27 ml. In an approximately 3D hemiarray case, volume prediction was possible with a maximum uncertainty of around 38 ml in the centre of the electrode plane. After application of a QI normalizing filter, average uncertainties in a two-dimensional hemiarray case were reduced to about 15 ml. Uncertainties in the approximate 3D case were reduced to about 30 ml.

Keywords: electrical impedance tomography, intraperitoneal haemorrhage, electrode array

(Some figures in this article are in colour only in the electronic version)

1. Introduction

Electrical impedance tomography (EIT) has a distinctive strength in terms of its sensitivity and ability to detect real-time changes in body composition due to processes such as bleeding, breathing and gastric emptying (Sadleir and Fox 2001, Adler 1997, Nour 1995). The EIT inverse problem is ill-posed and sensitive to noise, and does not provide images of a near-anatomic quality like MRI or CT. However, a time series of EIT data can easily be obtained, and contains valuable functional information.

1.1. Intraperitoneal haemorrhage in blunt trauma

Important abdominal organs such as the liver and spleen are vulnerable to blunt trauma caused by motor vehicle accidents, falls or detonations. The primary cause of fatalities in intraperitoneal bleeding is hypovolaemic shock related to blood loss from the damaged organs. Identification of intraperitoneal haemorrhage is often challenging because it may not be apparent during the initial assessment and treatment period (Odling-Smee 1984). In younger patients (those under 30 years), vital signs such as pulse rate and blood pressure may remain at normal levels in spite of a large blood loss until it is too late to provide treatment to them (Sadleir and Fox 2001). One report (Helmi *et al* 2001) tracking about 13 000 automobile accident victims in Qatar between 1991 and 1995 found the overall mortality rate involving abdominal trauma to be 25%. In half of these cases, mortality was due to abdominal trauma alone, and all of these deaths were due to either liver or splenic injury.

If it can be measured, time series data providing both the total amount of abdominal bleeding and the bleeding rate are useful indicators to warn both of impending hypovolaemic shock, and the urgency of surgery to repair injuries. Further, bleeding rate may be used to classify patients in terms of their surgical priority in battlefield or mass-casualty applications.

Conventional medical modalities such as x-ray, CT and MRI or ultrasound are presently unable to estimate bleeding rate or total blood loss (Sadleir and Fox 2001). Moreover, these methods are not well-suited to monitor bleeding continuously from accident to treatment site as they are either inconvenient for continuous use and cannot readily be made portable (x-ray, CT, MRI) or require expert interpretation (ultrasound).

1.2. Application of EIT to abdominal monitoring

Impedance images can potentially distinguish free blood because blood conductivity is relatively high compared with other tissues in the abdomen (Brown 2003). Sadleir and Fox (1998, 2001) showed that blood-like contrasts could be detected and quantified both *in vitro* and *in vivo* using a 16-electrode circumferential array and a linearized backprojection method. Such a method could be a valuable addition to critical care management. However, clinicians are reluctant to use new technology in a critical care environment if it is not convenient. For example, patients with blunt trauma may also have undetected spinal injuries, which could be aggravated if the patient is lifted to apply a monitoring device. Therefore, it is desirable to develop methods that do not involve applying electrodes underneath a supine patient.

1.3. The hemiarray topology

In this study, a novel electrode configuration for EIT was used to simplify the application of electrodes to supine patients. The hemiarray consists of a set of eight equally spaced electrodes in a semi-circular profile, applied to the anterior abdominal surface. Restricting the electrode

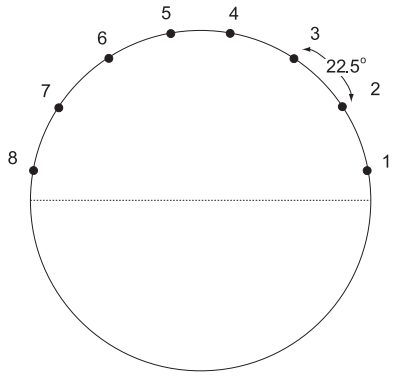

Figure 1. The hemiarray layout.

set to only the anterior abdominal surface avoids the need to lift patients and therefore risk further injury.

This topology falls halfway between the conventionally used arrays consisting of a number of electrodes equally spaced around the perimeter of an object, and planar arrays applied to a semi-infinite volume similar to those used in geophysics (for example, Avants (1999), Xu and Noel (1993)); other EIT applications (Mueller *et al* 1999); magnetic induction tomography (Igney *et al* 2005) and industrial process tomography (York *et al* 2005). Such configurations are challenging because of their lack of sensitivity to deep-lying anomalies.

In this paper we describe methods we used to reconstruct and quantify data gathered using hemiarrays, and contrast the results we obtained with data from standard eight- and 16-electrode arrays. In our study, we chose to use a current injection pattern similar to those used for standard arrays in order to more closely compare their properties. We performed experiments with cylindrical phantoms containing different volumes of blood-equivalent anomalies to study reconstruction and image quantity characteristics. These data were then evaluated to determine how well the hemiarray could determine bleeding rates.

2. Materials and methods

2.1. Full and hemiarray electrode configurations

The hemiarray electrode layout is shown in figure 1. It consists of eight electrodes separated by angles of 22.5° on a disc perimeter. This arrangement was used as it has the same electrode *spacing* as the commonly used 16-electrode EIT layout (Holder 2005) and thus can be directly compared with this layout's performance. The adjacent current and measurement pattern topology often used with EIT systems was employed with the hemiarray. In the adjacent pattern, currents are applied between adjacent-numbered pairs of electrodes (for example, 1–2) and differential voltage measurements are made between electrodes not involved in current application (3–4, 4–5, etc). In the hemiarray, use of this scheme included measurements and current applications between the last-numbered (8th) and first electrodes, positioned at distal ends of the array and approximately 160° apart. Excluding voltage measurements that include current electrodes, an N-electrode hemiarray has $N \times (N-3)/2$ independent measurements. For $N = 8$ there are 20 independent measurements. Eight-electrode hemiarray results were

compared to those obtained with an array consisting of eight or 16 electrodes equally spaced on the object perimeter (a 'full array').

The resolution obtained by the hemiarray topology is intrinsically limited by the electrode locations and number, and varies greatly depending on the location of objects relative to the electrode set. This is an intrinsic property of the layout. It may be possible to improve the signal-to-noise ratio in data using other current and voltage measurements than the adjacent one (Isaacson 1986), but the adjacent pattern includes all independent data that can be obtained using this electrode set.

2.2. Reconstruction and quantification methods

Because the abdomen is approximately cylindrical (or elliptical) in profile, and it is possible to extend electrodes axially to make the field distribution within the abdomen approximately two dimensional, we generally chose to assume the problem was two dimensional and to reconstruct conductivity distributions using a 2D disc model. We created a 2D static electrical finite element model of the hemiarray in Comsol Multiphysics (Comsol, Burlington, MA, USA). The model consisted of a fine mesh of approximately 28 000 triangular elements. In each element, the sensitivity (or Jacobian) of each measurement to a change in its conductivity was calculated for each current position using the method of Geselowitz and Lehr (Geselowitz 1971, Lehr 1972), by calculating lead fields in each pixel and computing, for each pixel, p, and measurement, i the quantity

$$S_{ip} = 1/(I_\phi I_\psi) \int_{dV_p} \nabla V_\phi \cdot \nabla V_\psi \, \mathrm{d}V_j, \tag{1}$$

where ∇V_ϕ and ∇V_ψ are field gradients within the element formed by using either the current application pair or voltage measurement pair involved in measurement i as sources, respectively. A three dimensional model consisting of about 16 000 tetrahedral elements was also created and used in a subset of reconstructions.

The condition numbers of both sensitivity matrices were of the order of 3×10^{17}.

Solutions to the inverse problem for changes in conductivity distribution were performed by the calculation of an approximate inverse for the sensitivity matrix, that is, by inverting the expression

$$\mathbf{dV} = \mathbf{S}\,\mathbf{d}\sigma \tag{2}$$

where $\mathbf{d}\sigma$ is the $TP \times 1$ conductivity change vector, $\mathbf{dV}$ is the $TM \times 1$ data vector and $\mathbf{S}$ is the $TM \times TP$ sensitivity matrix. Because the sensitivity matrix was ill-conditioned and not square, pseudoinversion was achieved using truncated singular value decomposition. We found that reconstruction quality improved when the sensitivity matrix was weighted with a diagonal matrix of reciprocal norms of sensitivity matrix columns (weighted minimum norm method) (Clay and Ferree 2002). In this method, images were obtained as

$$\mathbf{d}\sigma = \mathbf{W}(\mathbf{SW})^\dagger \, \mathbf{dV} \tag{3}$$

where $\mathbf{S}^\dagger$ denotes pseudoinversion. Entries in the $TP \times TP$ diagonal weighting matrix $\mathbf{W}$ were calculated via

$$W_p = \left(\sum_{i=1}^{TM} S_{ip}^2 \right)^{-1/2}. \tag{4}$$

The condition numbers of the $\mathbf{SW}$ matrices were around 1×10^{17}, somewhat smaller than the original $\mathbf{S}$ matrix.

Truncation values were selected by *l*-curve inspection (Hansen and O'Brien 1994). The *l*-curve method attempts to select an appropriate truncation value by plotting the image norm ($\|\mathrm{d}\sigma\|_2$) against the norm of the data residual ($\|S\mathrm{d}\sigma - \mathrm{d}V\|_2$) for many different truncation values, where $\|\cdot\|_2$ denotes the 2-*norm*. Conventionally, the optimal truncation value is selected by fitting a spline to the curve and finding the point of maximum curvature. The corner was selected at the truncation value *k* closest to this point (Hansen 1993). We used this method as a guide, but also found that the *k* values selected by this procedure occasionally produced values not at the point of maximum curvature as estimated by viewing the *l*-curve plot. The truncation value (*k*) used depended on the data noise level (Rust 1998). In phantom experiments, truncation values were chosen after inspecting images reconstructed at the truncation recommended by the *l*-curve procedure. If images with the recommended value were considered reasonable, further reconstructions for the data set were made using this value. If not, another value was chosen with reference to the *l*-curve plot. If this *k* value did not produce reasonable images, the value was decreased until images were considered clear and stable. Truncation values of 16 were typically used with phantom data, and the full rank of 20 used with synthetic data. For 3D phantom data, truncations at 12 or lower were necessary.

2.2.1. The quantity index. It is important to find an EIT image parameter that correlates with anomaly volume. One such image parameter used previously is the resistivity index (RI) (Sadleir and Fox 1998) defined as

$$\mathrm{RI} = \sum_{p=1}^{TP} \Delta r_p \tag{5}$$

for the case of a linearized backprojection reconstruction (Barber and Brown 1986), where the reconstructed distribution is log resistivity. This definition is valid for the case considered in Sadleir and Fox (1998), where equal area square pixels were used. A more exact definition of this parameter is the 'quantity index' (QI), which is the integral or discrete sum of the reconstructed conductivity or resistivity multiplied by pixel area or volume. In the case of conductivity distributions, we define QI as

$$\mathrm{QI} = \sum_{p=1}^{TP} \mathrm{d}\sigma_p \, \mathrm{d}A_p \tag{6}$$

with QI measured in units of S m (in two dimensions) or S m^2 (in three). Because reconstructions performed in this work involve a two-dimensional forward model, we quote QI in units of S m.

2.2.2. Quantity index normalization. The nonlinearity of the inverse problem leads to spatial variability in the point spread function of reconstructed anomalies. This variation is particularly large in the hemiarray case. QI is also affected, though to a lesser extent than peak pixel values or FWHM of reconstructed objects (Sadleir and Fox 1998). Methods that reduce spatial variation in QI will produce more accurate estimations of anomaly volume regardless of location. In this work, we implemented QI normalization by post-multiplying the matrix **SW** of (3) by a diagonal weighting matrix *Q*, and forming images via

$$\mathbf{d}\sigma = \mathbf{QW}(\mathbf{SWQ})^{\dagger}\,\mathbf{dV}. \tag{7}$$

The weighting matrix diagonal entries Q_p were calculated by determining the QI of each pixel spread function (PSF) in turn, using the column of the sensitivity matrix corresponding

to that pixel as the input data ('ideal' data). The truncation value chosen in obtaining the diagonal matrix was 20. Postmultiplying the SW matrix by Q resulted in a further decrease in condition number to 4×10^{16}.

Thus we have that denoting the PSF as $\hat{\sigma}^j$

$$Q_j = \sum_{p=1}^{TP} \hat{\sigma}_p^j \, \mathrm{d}A_p, \tag{8}$$

where

$$\hat{\sigma}^j = \mathbf{S}^\dagger \, \mathrm{col}(S_j). \tag{9}$$

The effect of this normalization filter is similar to that of a standard inverse filter, where an image is divided by the inverse of the imaging system's PSF (or in this case, its area weighted sum), and where the PSF has been thresholded to avoid dividing by near-zero values; then restored by multiplication (Gonzalez and Woods 2007). In our case, thresholding has been achieved by taking advantage of truncated singular value decomposition in the computation of $(\mathbf{SWQ})^\dagger$.

2.3. Reconstruction and quantification using synthetic data

The ability of the hemiarray topology to image and quantify objects at different positions in the disc plane was evaluated using 'ideal', model and phantom data. Ideal data consisted of columns of the sensitivity matrix. These data corresponded to the linearized data derived by placing an anomaly in a single pixel of the image plane. Evaluation of reconstruction and quantification characteristics for these data shows the best possible results, but does not give any real indication of the method's robustness. Data were also obtained from 2D finite element models (about 20 000 quadratic triangular elements) of discs containing anomalies (relative radius 0.2, conductivity twice the background) at relative radial positions 0, 0.2, 0.4, 0.5 and 0.8 from the centre in each of five directions. Reconstructions of these data with and without different amounts of added noise were used to determine the method's stability.

2.4. Experimental setup

Measurements from a phantom abdomen in conjunction with an eight-electrode EIT system were gathered to determine the potential of this configuration to provide good *in vivo* results.

The data acquisition module used to obtain phantom measurements, the EPack, is a prototype eight-electrode EIT system intended for use in emergency medicine and battlefield situations (Tang *et al* 2006). The device is controlled by a single digital signal processor (ADSP2181, Analog Devices). The processor configures a direct digital synthesizer (AD9850, Analog Devices) that in turn is the signal source for a 2 mA peak-to-peak dual Howland-type current source (Bertemes-Filho *et al* 2004). The source can be programmed to operate at one of several frequencies. In this work we operated the source at 62.5 kHz. Voltage difference signals measured by the system are amplified, and digitized by a 14-bit ADC (AD9240, Analog Devices). Waveforms are then sampled synchronous with the source, at 32 samples per cycle. The average rms value of each measured voltage waveform is calculated over 250 cycles. To offset the effects of the current source's finite output impedance we measured both the rms current (via the voltage developed across a precision resistor) and voltage measurement amplitude, and use the quotient of these as a measure of each transfer voltage or impedance $\mathbf{dV}_i$. The measurement precision of the system was better than 0.2% (Tang *et al* 2006).

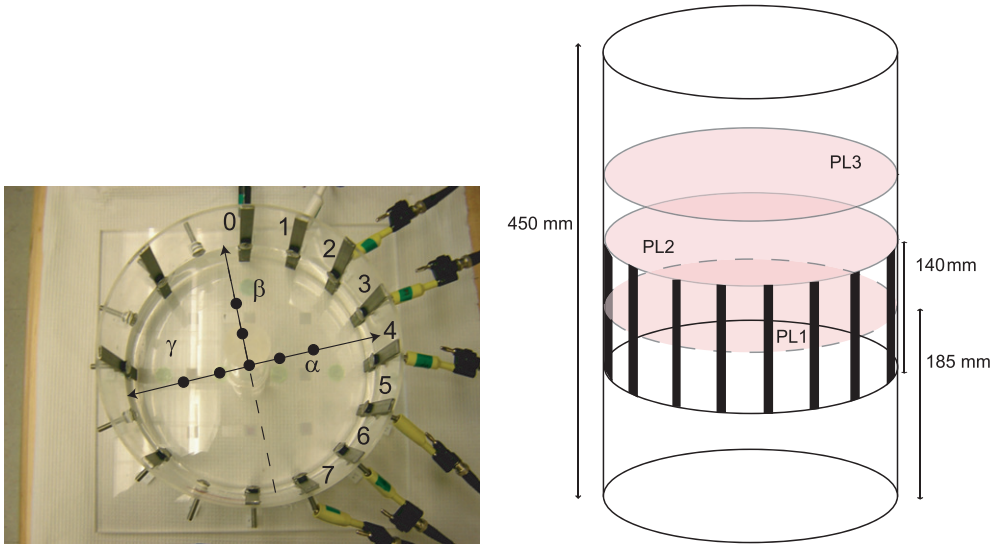

Figure 2. (Left) anomaly location map. Anomalies were positioned at relative radial locations of 0.25 and 0.5 in the alpha, beta and gamma directions as well as at the centre, a total of seven positions. When the full array was used anomalies were positioned at relative radii of 0, 0.25 and 0.5 only. (Right) plane location map. Anomalies were positioned at the centre and relative radial locations of 0.25 and 0.5 in planes PL1, PL2 and PL3 placed, respectively, at the centre of the electrode plane, one half, and one full electrode length away from the electrode plane.

Two cylindrical polycarbonate phantoms were used in the study. To obtain approximately two-dimensional data, we used a phantom with 260 mm diameter and 146 mm height, and electrodes (12 mm width) with the same height as the tank (shown from above in figure 2 (left)). A 0.2 Ω m saline solution (approximately 1 g l^{-1} NaCl) was used as the background solution. This conductivity was chosen because it is the approximate average conductivity of abdominal tissue (Sadleir and Fox 1998). Three-dimensional data were obtained using a taller phantom (269 mm diameter and 455 mm height, with the centre of the electrode plane at 185 mm height), and with shorter electrodes (12 mm width × 140 mm length) in order to determine the effect of axial position variation on reconstructions. In these studies, anomalies were placed in the same radial locations on three different planes, PL1, PL2 and PL3. PL1 was on the plane centre; PL2 was located approximately 70 mm, or half of one electrode length, from the electrode plane centre; and PL3 was located approximately 140 mm, or one electrode length, from plane centre, as shown in figure 2 (right). The aim in this case is to produce a uniform response in the quantity measure to anomaly volume in a large fraction of the abdomen, rather than to use small electrodes, where the response would be likely to be highly dependent on distance from the electrode plane.

Images of blood-like anomalies were gathered and post-processed to determine quantity indices. Blood-like anomalies with volumes between 25 and 200 ml were made using saline-doped TX-151 gels (Walker *et al* 2004, Sadleir *et al* 2006). The ability of the hemiarray and full array topologies to differentiate these anomaly volumes was compared. Figure 2 (left) shows hemiarray electrodes and the anomaly positions used. In the case of full array data, anomalies were positioned at relative radii of 0, 0.25 and 0.5 from the phantom centre. For

the 2D hemiarray case, anomalies were placed at seven different positions; these being at the same relative radial locations, but in directions towards (α), lateral to (β) and away from (γ) the electrode array. For the 3D hemiarray case the same directions as in the 2D hemiarray case were used, but relative radial locations of 0, 0.3 and 0.6 were used.

2.5. Phantom data comparisons

We compared mean values of QI (over all anomaly positions within the image plane) and the standard deviation of this quantity, to anomaly volume. Error bars on graphs show the standard deviation in the mean value for each volume, using data from all positions. Also plotted is a zero-intercept linear fit ($y = ax$) to the mean value obtained for each volume, with the proportion of variance accounted for by the linear fit (R^2) also shown. The fit function used was

$$\overline{\mathrm{QI}} = aV \tag{10}$$

where $\overline{\mathrm{QI}}$ is the estimated QI value, a is a constant (with units of S m ml^{-1} or S m^2 ml^{-1} depending on the model dimension). Specific points of comparison between the eight-electrode full array and hemiarray; and between two- and three-dimensional hemiarray cases, are detailed below.

2.5.1. Comparison of full array and hemiarray data. Reconstructions of two-dimensional eight-electrode full array and hemiarray phantom data were generated to permit a clear comparison of the image properties and quantity index characteristics of each. Blood-like anomalies with volumes of 50, 100, 150 and 200 ml were used. Reconstruction in full array cases was generated using the same fine mesh used to formulate hemiarray reconstructions and WMN (3).

2.5.2. Comparison of two-dimensional and three-dimensional hemiarray phantom reconstructions. The same two-dimensional reconstruction method was used to reconstruct tank data gathered in approximately two-dimensional (140 mm electrodes, 140 mm height tank) cases and for large tank 'three-dimensional' cases, where 140 mm bar electrodes were used in the tall tank. The same data described in section 2.5 were used for two-dimensional cases, and three-dimensional data were collected using blood-like anomalies of volumes 25, 50, 100 and 200 ml. Reconstructions for 3D cases were carried out using both 2D and 3D sensitivity matrices.

2.5.3. Correction of hemiarray spatial variance properties. For hemiarray cases only, correlations of two- and three-dimensional QI data were compared before and after normalization using QI data calculated using equations (7) and (8).

3. Results

3.1. Ideal and finite element model reconstructions and quantification

3.1.1. Unweighted reconstructions. Unweighted reconstructions of simulated data produced good representations of anomalies in the α direction, but diffuse images of anomalies in the β and γ directions. Figure 3(a) shows unweighted reconstructions of anomalies placed at relative radii of 0, 0.2, 0.4, 0.6 and 0.8 in the α, β and γ directions. The image at the top of each column is of the centrally placed anomaly, scaled to match those of reconstructions

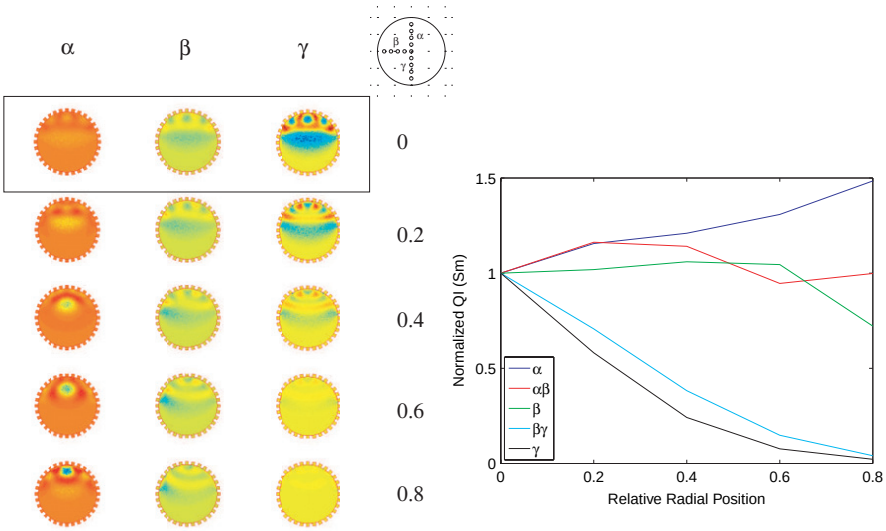

Figure 3. (a) Images of an anomaly (conductivity contrast 2, relative radius 0.05) as it is moved from the centre (top row) to a relative radius of 0.8 in the α (left column), β (middle column) and γ (right column) directions, for unweighted TSVD reconstructions. Colour scales of images in each column are the same. The image of the centrally placed anomaly at the top of each column shows the relation between colour scales. (b) QI of unweighted TSVD reconstructions of anomalies for each direction as a function of radial position. The $\alpha\beta$ and $\beta\gamma$ radial directions are half-way between the α and β and β and γ directions respectively. QI values are scaled relative to the QI of the central anomaly reconstruction; k is 20.

below. QI values increase by around 50% in the α direction and are reduced to around 2% of the central value in the γ direction, as shown in figure 3(b).

3.1.2. Weighted reconstructions. Weighted reconstruction produced generally superior images to the unweighted case. Figure 4(a) shows weighted reconstructions formed using the same data as in figure 3 and the reconstruction of (3). As in figure 3(a), the central anomaly reconstruction is shown at the top of the column for each direction, allowing relation of the colourscales used in each direction. An artefact is visible in the reconstruction of the highest α value anomaly. However, while the γ reconstructions are still quite diffuse, the anomalies are clearly visible on the linear colourscales. QI values for this case (figure 4) show a variation over all positions of around a factor of 4, the minimum value being around 40% of the central value and the maximum being 220%. Images of anomalies in the β-direction appear to be skewed towards the lower half of the plane at large radial displacements.

3.2. Phantom data reconstruction and quantification

3.2.1. Full array quantification. Figure 5 shows a plot of mean QI over the image plane against blood-equivalent anomaly volume for four anomaly cases. The error bars show the standard deviation in the mean value for each volume, using data from all four radial positions. Also plotted is the zero-intercept linear fit to the mean value obtained for each volume. The average volume uncertainty in this full array case was around 8 ml, with the maximum volume uncertainty for these cases in absolute volume equivalent terms being just under 10 ml.

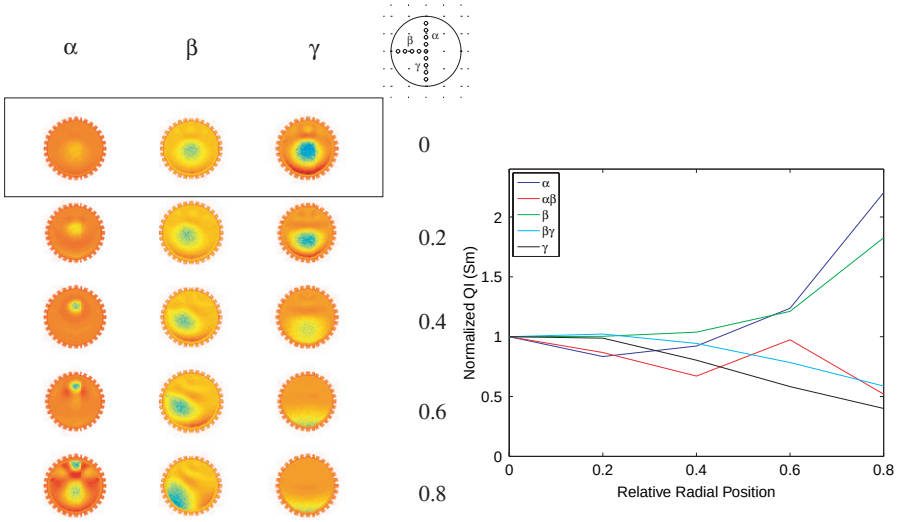

Figure 4. (a) Images of an anomaly (conductivity contrast 2, relative radius 0.05) as it is moved from the centre (top row) to a relative radius of 0.8 in the α (left column), β (middle column) and γ (right column) directions, for WMN TSVD reconstructions. Colour scales of images in each column are the same. The image of the centrally placed anomaly at the top of each column shows the relation between colour scales. (b) QI of WMN TSVD reconstructions of anomalies for each direction as a function of radial position. The $\alpha\beta$ and $\beta\gamma$ radial directions are half-way between the α and β and β and γ directions respectively. QI values are scaled relative to the QI of the central anomaly reconstruction; k is 20.

The largest coefficient of variation observed was around 7%. A linear (zero-intercept) fit to the data produced an R^2 value of 0.98.

3.2.2. Hemiarray images and quantification—2D. $\overline{\text{QI}}$ values and uncertainties from two-dimensional hemiarray reconstructions of blood-equivalent anomalies are shown in figure 6. The error bars showing standard deviations over the ten locations used are two to three times larger than those for the two-dimensional full array case. Average volume uncertainty was about 27 ml, with the maximum volume uncertainty in these data being around 38 ml and the 25 ml anomaly having a coefficient of variation over all positions of 58%. In percentage terms, the average coefficient of variation was less than 30% for all anomalies considered over all positions.

3.2.3. Hemiarray images and quantification—3D. Approximate three-dimensional configuration QI data are shown in figure 7. As expected, maximum sensitivity was observed in PL1, with the slope of the fit to the volume–$\overline{\text{QI}}$ curve decreasing to about half this value in PL3. The average coefficient of variation in PL1 was about 43%, nearly 50% larger than measured for the two-dimensional hemiarray case. In PL2, the average coefficient of variation was 70%. This observation was most likely due to effects of fringing fields near the electrode edges, as QI values in PL2 showed large variations from values obtained at locations close to electrodes when compared to corresponding cases seen in PL1, PL3 and in the 2D hemiarray case. The maximum volume uncertainty observed in PL1 was about 73 ml, and 94 ml in PL2, with maximum coefficient of variation of nearly 100%. The maximum observed coefficient

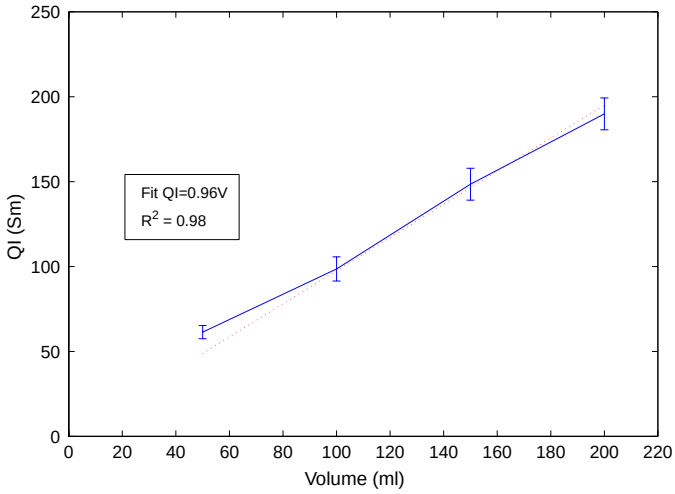

Figure 5. Plot of $\overline{\mathrm{QI}}$ against volume with standard deviations over four radial positions for eight-electrode full array reconstructions of blood-equivalent anomalies of 50, 100, 150 and 200 ml volume in a cylindrical phantom. A linear, zero intercept fit to the data produced a relation of $\overline{\mathrm{QI}} = 0.98$ V, with an R^2 value of 0.98. Average volume uncertainty was around 8 ml. A truncation value of 16 was used for these reconstructions.

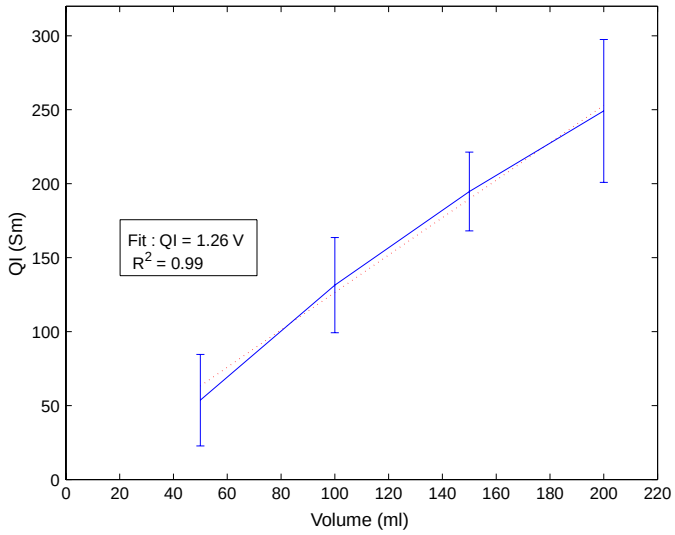

Figure 6. Plot of $\overline{\mathrm{QI}}$ against volume with standard deviations over ten positions for two-dimensional hemiarray reconstructions of blood-equivalent anomalies of 50, 100, 150 and 200 ml volumes in a cylindrical phantom. A linear, zero intercept fit to the data produced the relation $\overline{\mathrm{QI}} = 1.26$ V, with an R^2 value of 0.99. Average volume uncertainty in these data was around 27 ml over all positions. A truncation value of 16 was used for these reconstructions.

of variation in PL3 was only 22%, reflecting the smaller effect of moving the anomaly within a plane far from the main electrode field. The truncation value of 12 used in these cases was used after examining the *l*-curve for these data.

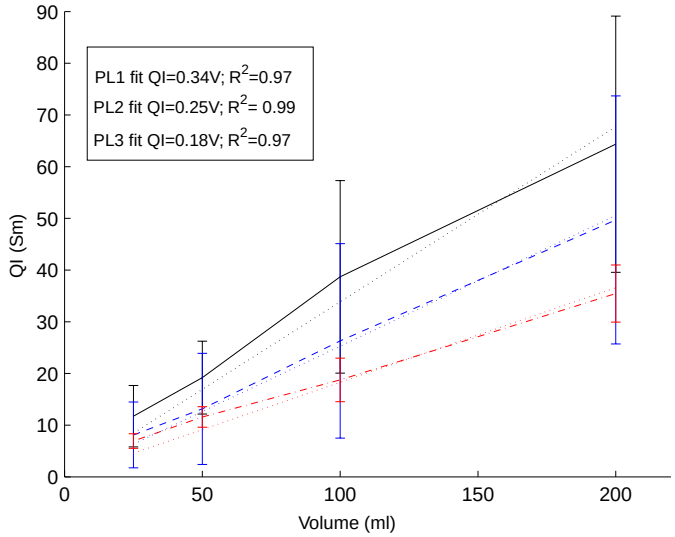

Figure 7. Plot of $\overline{\mathrm{QI}}$ against volume for hemiarray reconstructions of blood-equivalent anomalies of 50, 100, 150 and 200 ml volume in a cylindrical phantom. The curves show QI values and linear fits (dotted lines) to data for anomalies moved in (solid line) PL1, (dashed) PL2 and (dash-dot) PL3. A linear, zero-intercept fit to the PL1 data produced the relation of $\overline{\mathrm{QI}} = 0.34$ V, with an R^2 value of 0.97. The fit for PL2 data was $\overline{\mathrm{QI}} = 0.25$ V ($R^2 = 0.99$), and the fit to PL3 data was $\overline{\mathrm{QI}} = 0.18$ V ($R^2 = 0.97$). Maximum volume uncertainty in PL1 was about 73 ml, with maximum coefficient of variation of 50%. In PL2 (at the edge of the electrode plane) the maximum volume uncertainty was 94 ml, with a maximum observed coefficient of variation 80%. In PL3 volume uncertainty was a maximum of 30 ml in volume terms, with maximum coefficient of variation being 22%. A truncation value of 12 was used for these reconstructions because of the generally increased noise levels.

A three-dimensional reconstruction was also performed on these data. A 16 000 element 3D model was constructed with a similar axial height and electrode dimension to the experimental tank. Reconstructions using this model were also successful, with the relevant scaling factors a being 1.57 (for PL1), 1.22 (for PL2) and 0.60 (for PL3). Linear fits had poorer quality, with R^2 values for fits in each plane being 0.96, 0.97 and 0.98 in PL1, PL2 and PL3 respectively. Uncertainties were similar to those observed in 2D reconstructions, having average coefficients of variation 49%, 44% and 24% respectively. A truncation value of 10 was used in these reconstructions.

3.2.4. QI normalization of simulated data and hemiarray phantom data. QI normalization was applied to both simulated data (at a k value of 20) and two- and three-dimensional phantom hemiarray data sets at k values of 16 and 12 for the two- and three-dimensional data respectively. In simulated data, the effect of applying (7) was to produce QI values symmetrically distributed about the central value. The standard deviation was reduced only slightly. However, when applied to the two-dimensional phantom data, the effect of this normalization was to halve the average coefficient of variation from 30% to 14%. In three-dimensional phantom data the effect was similar, with a reduction of coefficient of variation in PL1 to 32%; in PL2 to 35%; and a slight increase to 24% in PL3.

4. Discussion

It is inevitable that a reduction in electrode number will lead to poorer image properties and an increased uncertainty in quantity estimations. Restricting electrodes to half the electrode plane further reduces overall image quality, increases spatial variance and therefore the variability in quantity estimates of an anomaly at an arbitrary location.

The large spatial variability observed in the hemiarray reconstructions (shown in figure 4(b)) was dominated by increases in the α direction. The standard deviations observed in hemiarray cases would be reduced if the upper half-plane (or some portion of it) were masked out in QI calculations. A practical approach incorporating such a method would also be reasonable, as bleeding in supine patients would be expected to accumulate in the posterior region of the peritoneum (paracolic gutters). In this study, we have included all the image plane in an effort to show worst case values and the limits of detection.

In an earlier phantom study (Sadleir and Fox 1998) of an approximately two-dimensional case, we observed an uncompensated standard deviation in quantity estimate of about 13% (out to a relative radius of 0.65) using a full array of 16 electrodes, an adjacent measurement scheme and linearized backprojection reconstruction. For the two 2D eight-electrode cases considered here, and using a weighted sensitivity matrix-based reconstruction, we observed a standard deviation of 10% in the full array topology; and a standard deviation of about 25% for the eight-electrode hemiarray. Further compensation of hemiarray image data using QI data reduced the standard deviation in the two-dimensional hemiarray setup to around 10%, and in the 3D setup to about 30%. Thus, the combination of a filtering technique with a more exact, and weighted, reconstruction method was able to significantly mitigate the effects of changing the electrode layout.

With a given system precision, it may be possible to increase the signal-to-noise ratio in data by choosing different current injection patterns (Isaacson 1986). However, the basic information contained in the data collected using this adjacent topology cannot be improved upon. Even with noiseless data, reconstructions towards the posterior part of the image are compromised. However, the minimum signal obtained using the hemiarray topology is actually larger than would be obtained using a conventional adjacent measurement pattern with 16 electrodes. This is because the smallest signal would be obtained immediately opposite the current electrode pair, whereas the hemiarray pattern does not have access to this measurement.

In the three-dimensional hemiarray experiment, the sensitivity of the system to blood-equivalent anomalies was reduced by a factor of about 2 as anomalies were moved in planes out to one electrode length from the centre of the electrode plane, similarly to results found in Sadleir and Fox (1998), where RIs reduced to about 60% of their central plane values at this distance.

It has been shown here that a straightforward compensation for PSF variation can produce much improved uncertainty in volume estimates. We are currently testing modifications of this approach, applied to both full array and hemiarray cases, to further improve QI value estimations.

It is clear that use of the hemiarray reduces the sensitivity and accuracy of volume change estimations. However, it is crucial to consider the capabilities of the imaging method in the context of the needs of clinicians in particular applications. Use of an array that does not require the patient to be lifted for its application (and does not require any additional hardware beyond a portable electrode belt and system) would be very convenient for emergency applications, and would promote its use. At the same time, the accuracy required in such situations is not extreme, because the detection of bleeding, and its subsequent monitoring, are more important than the precise quantities of blood involved. In an earlier work (Sadleir 2001) it

was estimated that a bleeding rate of 30 ml min^{-1} was not significant, and that a rate above 100 ml min^{-1} indicated bleeding requiring laparotomy. We estimate that a method that has an uncertainty that is as much as 50 ml (half this rate) would be suitable for blood detection. As the uncertainties found here were well below 100 ml, we believe that this method will be a viable one for detection of intraperitoneal bleeding even when the effects of breathing and motion-related artefacts are included.

Analysis of quantity and image data together would also greatly aid in diagnoses. Significantly, this method represents a shift in emphasis from approaches where images of individual anomalies are sought to one where quantitative information derived from images is the primary measure, and images are used as a secondary measure, for example, to verify electrode contact and confirm approximate bleeding locations. While four-electrode 'one pixel' techniques are similar in approach, namely a single parameter being used as an indication of a condition, these methods do not give spatial information and provide less scope to verify data quality.

In future work, we plan to test the method *in vivo* and determine the effects on sensitivity, images and quantity estimates of artefacts such as breathing and movement. Analyses will be performed of the effect of restricting quantity analysis to a more posterior region of interest.

5. Conclusion

A novel eight-electrode arrangement was tested for use in abdominal EIT for imaging and quantification. It was found that use of the topology resulted in increased uncertainty in quantity measures when quantification over the entire image plane was considered. The amount of uncertainty could be reduced by about half using a normalization factor related to the observed variation in quantity indices. The uncertainty was sufficiently low that the arrangement may be a feasible approach to monitoring and quantification of abdominal bleeding in the context of blunt trauma.

Acknowledgments

This work was supported in part by the US Army Medical Research and Materiel Command under award no. W81XWH-07-1-0591.

References

Adler A, Amyot R, Guardo R, Bates T J H and Berthiaume Y 1997 Monitoring changes in lung air and liquid volumes with electrical impedance tomography *J. Appl. Physiol.* **83** 1762–7

Barber D C and Brown B H 1986 Recent developments in applied potential tomography—APT *Information Processing in Medical Imaging* ed S L Bacharach (Dordrecht: Martinus Nijhoff)

Bertemes-Filho P, Lima R G and Amato M B P 2004 Capacitive-compensated current source used in electrical impedance tomography *Proc. 12th Int. Conf. on Electrical bioimpedance and 5th Conf. on Electrical Impedance Tomography (Gdansk, Poland, 20–24 June)* ed A Nowakowski

Brown B *et al* 2003 Electrical impedance tomography (EIT): a review *J. Med. Eng. Technol.* **27** 98–107

Clay M T and Ferree T C 2002 Weighted regularization in electrical impedance tomography with applications to acute cerebral stroke *IEEE Trans. Med. Imaging* **21** 629–37

Geselowitz D B 1971 An application of electrocardiographic lead theory to impedance plethysmography *IEEE Trans. Biomed. Eng.* **18** 38–41

Gonzalez R C and Woods R E 2007 *Digital Image Processing* 3rd edn (Reading, MA: Addison-Wesley)

Hansen P C 1994 Regularization tools: a Matlab package for analysis and solution of discrete ill-posed problems *Numer. Algorithms* **6** 1–35

Hansen P C and O'Leary D P 1993 Use of the l-curve in the regularization of discrete ill-posed problems *SIAM J. Sci. Comput.* **14** 1487–503

Helmi I, Hussain A and Ahmed A A H A 2001 Abdominal trauma due to road traffic accidents in Qatar *Inj, Int. J. Care Injured* **32** 105–8

Holder D C (ed) 2005 *Electrical Impedance Tomography. Methods, History and Applications* (Bristol: Institute of Physics Publishing)

Igney C H, Watson S, Williams R J, Griffiths H and Dossel O 2005 Design and performance of a planar-array MIT system with normal sensor alignment *Physiol. Meas.* **26** S263–78

Isaacson D 1986 Distinguishability of conductivities by electric current computed tomography *IEEE Trans. Med. Imaging* **5** 91–5

Lehr J 1972 A vector derivation useful in impedance plethysmography field calculations *IEEE Trans. Biomed. Eng.* **18** 156–7

Mueller J L, Isaacson D and Newell J C 1999 A reconstruction algorithm for electrical impedance tomography data collected on rectangular electrode arrays *IEEE Trans. Biomed. Eng.* **46** 1379–86

Nour S, Mangnall Y F, Dickson S J A, Johnson A G and Pearse R G 1995 Applied potential tomography in the measurement of gastric emptying in infants *J. Pediatr Gastroenterol. Nutr.* **20** 65–72

Odling-Smee W 1984 Abdominal injuries *Surgery* **15** 348–53

Rust B W 1998 Truncating the singular value decomposition for ill-posed problems *US Dep. Commer. Tech. Rep.* NITIR **6131** pp 1–36

Sadleir R J and Fox R A 1998 Quantification of blood volume by electrical impedance tomography using a tissue equivalent phantom *Physiol. Meas.* **19** 501–16

Sadleir R J and Fox R A 2001 Detection and quantification of intraperitoneal fluid using electrical impedance tomography *IEEE Trans. Biomed. Eng.* **48** 484–91

Sadleir R J, Grant S, Zhang S U, Oh S H, Lee B I and Woo E J 2006 High field MREIT: setup and tissue phantom imaging at 11 T *Physiol. Meas.* **27** S261–70

Tang T, Zhang S U and Sadleir R J 2006 A portable 8-electrode EIT measurement system *Proc. 7th Conf. on Biomedical Applications of EIT* pp 190–3

Walker G C, Berry E, Smye S W and Brettle D S 2004 Materials for phantoms for terahertz pulsed imaging *Phys. Med. Biol.* **49** N363–9

Xu B and Noel M 1993 On the completeness of data sets with multielectrode systems for electrical resistivity survey *Geophys. Prospect.* **41** 791–801

York T A, Davidson J L, Mazurkiewich L, Mann R and Grieve B D 2005 Towards process tomography for monitoring pressure filtration *IEEE Sens. J.* **5** 139–52

IOP PUBLISHING PHYSIOLOGICAL MEASUREMENT

Physiol. Meas. **30** (2009) 275–289 doi:10.1088/0967-3334/30/3/004

Normalization of a spatially variant image reconstruction problem in electrical impedance tomography using system blurring properties

Sungho Oh, Te Tang, A S Tucker and R J Sadleir

J Crayton Pruitt Family Department of Biomedical Engineering, University of Florida, Gainesville, FL, USA

E-mail: sausa@ufl.edu

Received 30 September 2008, accepted for publication 12 January 2009
Published 6 February 2009
Online at stacks.iop.org/PM/30/275

Abstract

The electrical impedance tomography (EIT) image reconstruction problem is ill posed and spatially variant. Because of the problem's ill-posed nature, small amounts of measurement noise can corrupt reconstructed images. The problem must be regularized to reduce image artifacts. In this paper, we focus on the spatially variant characteristics of the problem. Correcting errors due to spatial variance should improve reconstruction accuracy. In this paper, we present methods to normalize the spatially variant image reconstruction problem by equalizing the point spread function (PSF). In order to equalize the PSF, we used the reconstruction blurring properties obtained from the sensitivity matrix. We compared three mathematical normalization schemes: pixel-wise scaling (PWS), weighted pseudo-inversion (WPI) and weighted minimum norm method (WMNM) to equalize images. The quantity index (QI), defined as the integral of pixel values of an EIT conductivity image, was considered in investigating spatial variance. The QI values along with reconstructed images are presented for cases of two-dimensional full array and hemiarray electrode topologies. We found that a spatially invariant QI could be obtained by applying normalization methods based on equalization of the PSF using conventional regularized reconstruction methods such as truncated singular value decomposition (TSVD) and WMNM. We found that WMNM normalization applied to WMNM regularized reconstruction was the best of the methods tested overall, for both hemiarray and full array electrode topologies.

Keywords: electrical impedance tomography, spatially variant image reconstruction, point spread function, pixel-wise scaling, weighted pseudo-inversion, weighted minimum norm method, full array, hemiarray, quantity index

(Some figures in this article are in colour only in the electronic version)

1. Introduction

The human body is made of tissues that are well contrasted in electrical conductivity (Barber and Brown 1984). Therefore, an imaging modality such as electrical impedance tomography (EIT) that produces conductivity distribution information within the body may find useful clinical application. In EIT, a set of electrodes is positioned on the patient's skin. Low-amplitude currents are applied through a pair of electrodes, and the resulting surface voltages are measured. This procedure is repeated until we obtain all the possible independent measurements. The measurements are a function of the body's internal conductivity distribution. Therefore, cross-sectional conductivity images can be reconstructed from the measurements, given knowledge of the input current pattern and the patient's body shape. Images of conductivity changes may provide information about changes in physiological states. Thus, EIT has potential clinical applications as a real-time bedside monitor.

Potential limitations in performance of the EIT systems include that input current travels nonlinearly within the body, and its trajectory cannot be predicted precisely, and that the available information about the object is limited by the total number of electrodes, yet using many electrodes may not be practical in clinical settings. Consequently, we must pay special attention to the ill-posed nature and spatial variability of the EIT image reconstruction problem, which are mathematical embodiments of the above limitations. Due to its *ill-posed nature*, small measurement errors can impair reconstructed images. In this case, the problem must be regularized to return reasonable images. Further, the image reconstruction problem is *spatially variant*, meaning that the same anomaly may produce different reconstruction signatures depending on its location within the image plane. In this case, regularization methods may still produce inaccurate reconstructions. Therefore, we diagnose spatial variability as a critical problem that needs resolution.

As a consequence of spatial variability, estimated quantities of conductive anomalies will also appear to vary according to their positions (Sadleir and Fox 1998). In EIT monitoring of lung air and liquid volume changes, Adler *et al* (1997) also reported quantification errors that depended on radial positions of anomalies. Spatial variance may not be a significant problem when the region of interest (ROI) is relatively small. For example, in Blott *et al*'s study (2000) of simulated two-dimensional intra-ventricular haemorrhage, quantitation errors due to spatial variance of reconstructions were likely negligible for that reason. However, in other applications such as detection of intra-peritoneal bleeding, determining an ROI is not straightforward, because bleeding may occur over a large fraction of the imaged domain. Therefore, reducing spatial variability is desired to improve accuracy in estimating anomaly quantities.

In this paper, we used reconstruction blur analysis in order to reduce errors caused by spatial variance. We demonstrate that normalizing the point spread function (PSF) by its integral can result in a spatially invariant quantity index (QI). We considered the PSF to be the reconstruction (or blurring) of single-element (pixel) anomalies. Cohen-Bacrie *et al* (1997) used variance of this PSF as penalty term in Tikhonov regularization. In this paper, we used the integral of PSF functions as normalizing terms. Three mathematical frameworks of normalization were compared: *pixel-wise scaling (PWS)*, *weighted pseudo-inversion (WPI)* and *weighted minimum norm method (WMNM)* for two-dimensional eight-electrode 'full array' and 'hemiarray' reconstructions. Data were obtained from numerically simulated two-dimensional disk models (Comsol Multiphysics: Burlington, MA) containing simulated disk anomalies placed at various locations in the image plane and a cylindrical saline phantom containing blood-like anomalies in a less-conducting background.

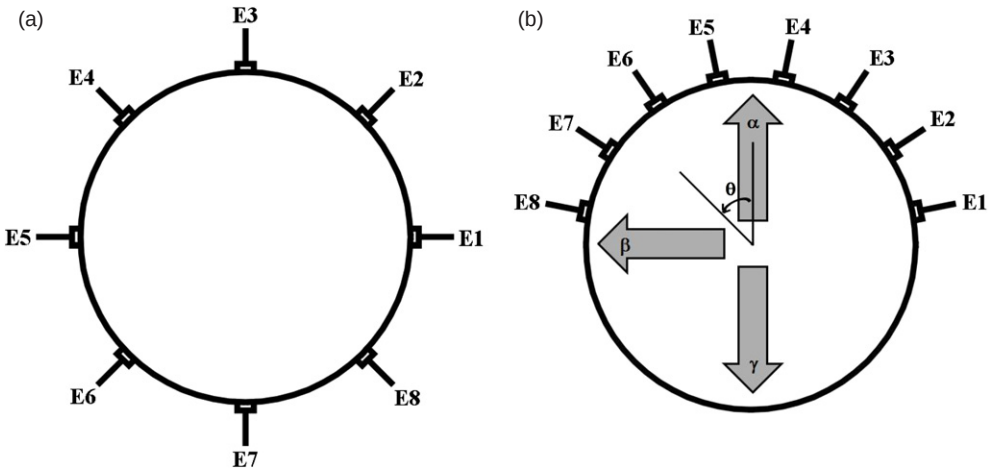

Figure 1. Illustration of eight-electrode arrays applied to the boundary of a disk object. Electrodes are labeled by indices E1, E2, . . . , E8. (a) Full array electrode layout. (b) Hemiarray electrode layout. The variable θ represents clockwise angular displacement away from the north pole. Directions at θ values of 0, 90 and 180° were denoted as α, β and γ, respectively.

2. Methods

2.1. Forward problem

Given an object Ω, input current is transmitted through the object boundary $d\Omega$, which is assumed smooth. A corresponding electric potential Φ is generated following the Laplace equation (1*a*) with boundary conditions (1*b*) for conductivity σ, which is a function of position:

$$\nabla \cdot (\sigma \nabla \Phi) = 0 \quad \text{in } \Omega, \text{ subject to} \tag{1a}$$

$$\sigma(x, y, z)(\partial \Phi / \partial n) = -J \quad \text{on } d\Omega, \tag{1b}$$

where J is the current density prescribed on the object boundary, and n is a unit outward normal to the surface.

2.2. Full array and hemiarray topologies

In a conventional EIT electrode topology, electrodes are spaced equidistantly around the entire object boundary. This ensures current projections are axially symmetric within the assumed object shape. We call this the full array (figure 1(a)). The novel hemiarray electrode layout (figure 1(b)) is motivated by clinical requirement to place electrodes only on the anterior surface of the body (Sadleir *et al* 2008). Although there are practical advantages over the full array, the hemiarray forms current projections that are highly asymmetric with respect to the image plane, worsening the spatial variability of reconstructions.

2.3. Adjacent electrode measurement

A standard adjacent electrode configuration was employed for both full array and hemiarray topologies. In the adjacent electrode configuration (Malmivuo and Plonsey 1995), a neighboring pair of electrodes is used to inject input currents. Other electrode pairs, excluding the current pair, are used to make adjacent boundary voltage measurements. The following

Table 1. Properties of the sensitivity matrices **S** of eight-electrode full array and hemiarray topologies.

	Full array	Hemiarray
Dimensions	40×344	40×344
Rank	20	20
Condition number	2.21×10^{17}	2.02×10^{18}

adjacent pair of electrodes is chosen for the next current injection, and the next set of adjacent boundary voltage measurements is made. This procedure is repeated until all the possible adjacent pairs are tried. For n electrodes, adjacent electrode configuration produces $n \times (n-3)$ measurements in total. Therefore, using eight electrodes produces 40 measurements in total. Among these, only 20 measurements are independent due to reciprocity (Malmivuo and Plonsey 1995).

2.4. Inverse problem

In EIT image reconstruction, the conductivity distribution within an object is estimated from measured boundary voltage, given input current patterns and an object shape. We used a linearized reconstruction problem given by (2), where the conductivity change $\Delta\sigma$ (dimension $N \times 1$, where N is the total number of pixels (elements) in the image plane) is to be estimated from a reference condition (Lionheart 2004):

$$\Delta V = \mathbf{S}\Delta\sigma. \tag{2}$$

Here, ΔV ($M \times 1$, where M is the total number of measurements) is the change of voltage measurement from a reference measurement, and $\mathbf{S}$ ($M \times N$) is the sensitivity matrix. Reference measurements were made on a disk model that contains a homogenous background medium (Meeson *et al* 1995). Each entry $\mathbf{S}_{ij}$ in $\mathbf{S}$ is the sensitivity (i.e. amount of voltage change expected) of measurement i to a unit conductivity change in element j (Lionheart 2004).

The image plane used throughout this paper had 344 elements. Excluding elements that lay on the boundary, all elements were square and had the same area. In table 1 the properties of **S** calculated for this plane are summarized for both eight-electrode full array and hemiarray cases. **S** was a rectangular matrix for our image plane, which made (2) an underdetermined problem. The large condition numbers indicate that equation (2) is an ill-posed inverse problem that must be regularized to obtain reasonable solutions. According to table 1, the hemiarray sensitivity matrix has a larger condition number than the full array for the same number (eight) of electrodes.

2.5. Truncated singular value decomposition

In order to invert (2) and obtain $\Delta\sigma$, singular value decomposition (SVD) can be used to calculate the pseudo-inverse of the sensitivity matrix $\mathbf{S}^+$ as in (3):

$$\mathbf{S}^+ = \mathbf{V}\mathbf{D}^+\mathbf{U}^T. \tag{3}$$

Here, **U** and **V** are unitary matrices whose columns are the left and right singular vectors of **S**. $\mathbf{D}^+$ is a truncated inverse of the singular value matrix. Obtaining an estimated conductivity solution $\Delta\hat{\sigma}$ of (2) using $\mathbf{S}^+$ as the reconstruction matrix is termed truncated SVD (TSVD) (4). TSVD was proposed for discrete ill-posed problems by Hansen (1987) to achieve smooth solutions:

$$\Delta\hat{\sigma} = \mathbf{S}^+\Delta V. \tag{4}$$

Once the reconstruction vector $\Delta\hat{\sigma}$ is calculated, images can be made by simply assigning entries of $\Delta\hat{\sigma}$ to their corresponding elements in the image plane. The estimated solution $\Delta\hat{\sigma}$ can be expressed as the weighted sum of rank-1 matrices as in (5):

$$\Delta\hat{\sigma} = \sum_{i=1}^{k} \frac{u_i^T \Delta V}{d_i} v_i, \tag{5}$$

where k is termed the regularization parameter (or truncation number in TSVD) and can be chosen based on the amount of noise in the measurement ΔV (Hansen 1987).

2.6. L-curve criterion

Determination of the regularization parameter is not straightforward, since the noise quantity is generally unknown. Hansen (1992) suggested the use of the *l*-curve in selecting adequate regularization parameters. In the *l*-curve, solution norm of the problem is plotted versus residual norm in the log–log scale. The resulting curve is usually L-shaped with a corner, hence its name. In this paper, we examined the *l*-curve for each reconstruction and chose the minimum k value (5) corresponding to the corner determined by visual inspection to reconstruct all data.

2.7. Weighted minimum norm method (WMNM)

WMNM has been implemented in EIT image reconstruction as a way to resolve the problems arising from low sensitivity (Clay and Ferree 2002). In WMNM, columns of the sensitivity matrix are equalized in terms of its power before pseudo-inversion and recovered by rescaling the pixels. The final form of WMNM is displayed in (6):

$$\Delta\hat{\sigma} = \mathbf{W}(\mathbf{SW})^{+}\Delta V, \tag{6}$$

where the weighting matrix $\mathbf{W}$ ($N \times N$) is a diagonal matrix whose terms (w_j) are defined as in (7):

$$w_j = \left(\sum_{i=1}^{M} S_{ij}^2 \right)^{-1/2}, \qquad j = 1, 2, \ldots, N. \tag{7}$$

2.8. Quantity index (QI)

At an early stage of EIT's development, Barber (1990) suggested that a volume integral of relative resistivity changes in reconstructed images may be a useful quantitative measure. Here, we propose integrals of EIT images as a useful measure to estimate changes of anomaly volume. The quantity defined in (8) is termed the QI. QI can be thought of as the average of the conductivity change $\Delta\sigma$ multiplied by the number of elements N:

$$\mathrm{QI} = \sum_{j=1}^{N} A_j \cdot \Delta\sigma_j. \tag{8}$$

For an element (or pixel) j, the conductivity change and element area are denoted as $\Delta\sigma_j$ and A_j, respectively.

The relative QI (δQI) for a reference QI (where QI_0 is that calculated from the anomaly located at the domain center) is defined in (9):

$$\delta\mathrm{QI} = \mathrm{QI}/\mathrm{QI}_0. \tag{9}$$

2.9. Point spread function (PSF) and blurring

In order to investigate blurring in EIT image reconstruction, we introduce the PSF. Consider a unit conductivity change in an element (pixel) j within the image. This unit change can be expressed in a vector form as an entry of 1 in the jth position and zeros elsewhere ($[0 \quad \dots \quad 0 \quad 1 \quad 0 \quad \dots \quad 0]^T$). The weighted sum of these vectors is a vector form of the *ideal image*. The change in boundary voltage measurements subject to this unit conductivity change is the jth column of the sensitivity matrix **S**. Ideally any measurement can be represented as a weighted sum of sensitivity matrix columns. Therefore, the column space of **S** can be termed the *ideal measurement* space. By reconstructing from the ideal measurements, a blurred version of the ideal element (pixel) image is obtained, which we term the PSF:

$$\delta_j = \mathbf{B}[0 \quad \dots \quad 0 \quad 1 \quad 0 \quad \dots \quad 0]^T, \tag{10}$$

where **B** ($N \times N$) is the blurring matrix and δ_j is the PSF vector for an anomaly in the jth element. The column space of **B** is a blurred version of the ideal images. The blur matrix **B** is defined as the product of the sensitivity matrix and the reconstruction matrix. Therefore, it can be easily obtained for reconstruction matrices that are expressed in algebraic form. In (11*a*) and (11*b*), definitions of the **B**s are displayed in the context of TSVD and WMNM regularization, respectively. One can also easily obtain **B** for other regularization methods such as Tikhonov regularization:

$$\mathbf{B} = \mathbf{S}^+\mathbf{S}, \tag{11a}$$

$$\mathbf{B} = \mathbf{W}(\mathbf{SW})^+\mathbf{S}. \tag{11b}$$

We are interested in using the properties of **B** to normalize spatially variant image reconstruction problems. When normalizing such problems, the unit of the reconstructed quantity should be preserved after normalization (Barber 1990). Entries in **B** are dimensionless (10). Therefore, reconstruction quantities after normalization have the same units as quantities before normalization. In (12), the column sum of **B** is defined as q_j:

$$q_j = \left(\sum_{i=1}^{N} \mathbf{B}_{ij}\right), \qquad J = 1, 2, \dots, N. \tag{12}$$

The normalization matrix used throughout this paper is defined as **Q** ($N \times N$) in (13), which is a diagonal matrix whose entries are q_j's:

$$\mathbf{Q} = \begin{bmatrix} q_1 & 0 & \cdots & 0 \\ 0 & q_2 & 0 & \vdots \\ \vdots & 0 & \ddots & 0 \\ 0 & \cdots & 0 & q_N \end{bmatrix}. \tag{13}$$

2.10. Eigenimages

Using SVD, we can estimate basis images that determine the system blurring **B** (*eigenimages*). It is clear from (14) that columns of the right singular matrix **V** can be seen as eigenimage vectors:

$$\mathbf{B} = \mathbf{S}^+\mathbf{S} = (\mathbf{UDV}^T)^+(\mathbf{UDV}^T) = \mathbf{VD}^+\mathbf{DV}^T = \mathbf{V}\begin{bmatrix} \mathbf{I}_k & \mathbf{0} \\ \mathbf{0} & \mathbf{0} \end{bmatrix}\mathbf{V}^T, \tag{14}$$

where $\mathbf{I}_k$ ($k \times k$) is the identity matrix. It is also clear in (14) that the blurring depends on the truncation number k.

2.11. Pixel-wise scaling (PWS)

Thomas *et al* (1994) used a method that scaled log-resistivity images pixel-wise in order to reduce variation in quantity estimates. We can also apply PWS to our case in which conductivity change is to be reconstructed. In (15), PWS is presented in a matrix form:

$$\Delta\hat{\sigma} = \mathbf{Q}^{-1}\mathbf{S}^{+}\Delta V. \tag{15}$$

A more advanced method was proposed by Sadleir and Fox (1998), who demonstrated a post-reconstructive filtering method that combined PWS and conformal transformations. In their work, the maximum spatial error in quantitation from phantom experimental results decreased from 30% to 6%. However, a large region near the object boundary (normalized radius $>$ 0.75) was excluded from quantification.

2.12. Weighted pseudo-inversion (WPI)

The normalization that we use here is WPI. The normalized reconstruction can be obtained by weighting columns of the sensitivity matrix by terms in **Q** prior to reconstruction as in (16):

$$\Delta\hat{\sigma} = (\mathbf{SQ})^{+}\Delta V. \tag{16}$$

If **SQ** is a full-rank matrix, (16) will become identical to (15). In this vein, we speculate that WPI should normalize the reconstruction in a similar way to PWS, with an additional advantage of using the truncated pseudo-inverse.

2.13. Normalization in the framework of WMNM

In the work of Oh and Sadleir (2007), a WPI method was shown to decrease spatial variance of the QI. However, the normalized reconstruction $\Delta\hat{\sigma}$ in (16) did not produce reasonable images. To obtain meaningful images, one can borrow the mathematical framework of WMNM, which can be done by multiplying **Q** post-reconstructively. The final form is shown in (17):

$$\Delta\hat{\sigma} = \mathbf{Q}(\mathbf{SQ})^{+}\Delta V. \tag{17}$$

It was also noticed that using the WMNM framework can introduce normalization effects in some cases. Sadleir *et al* (2008) used a combined method of WMNM regularization (11) and WMNM normalization (17) in the eight-electrode hemiarray case, which produced normalized QIs and images. The matrix equation of this normalized reconstruction method is shown in (18):

$$\Delta\hat{\sigma} = \mathbf{QW}(\mathbf{SWQ})^{+}\Delta V. \tag{18}$$

2.14. Computer simulation

Two-dimensional forward models of a disk (r_d) containing a single internal anomaly (r_a) at various locations were designed and solved using Comsol Multiphysics (Burlington, MA) and Matlab. We tested two types of models with anomaly locations as shown in figure 1. The full array model had eight boundary electrodes placed equidistantly. The hemiarray model had eight electrodes placed on the anterior boundary only. All electrodes had the conductivity of copper (6×10^7 [S m^{-1}]). The length of each electrode was 0.1 relative to the disk radius, subtending an angle of 5.7° on the disk perimeter. The models were discretized to 1374 second-order triangular finite elements, and then solved for boundary voltage values subject to adjacent input current patterns using the direct linear system solver UMFPACK (Unsymmetric MultiFrontal PACKage). The anomaly had a radius $0.1 \times r_d$ and was centered at locations

Table 2. Index assignment for various normalization methods. The methods are represented by reconstruction matrices. The normalization matrices $\mathbf{Q}_t$ and $\mathbf{Q}_w$ were calculated using (11*a*) and (11*b*) respectively. Methods A1–A4 are based on TSVD reconstruction (9), and methods B1–B4 and C5 are based on WMNM reconstruction (11).

Index	Normalization method	Reconstruction matrix
A1	None	$\mathbf{S}^+$
A2	PWS	$\mathbf{Q}_t^{-1}\,\mathbf{S}^+$
A3	WPI	$(\mathbf{S}\mathbf{Q}_t)^+$
A4	WMNM	$\mathbf{Q}_t(\mathbf{S}\mathbf{Q}_t)^+$
B1	None	$\mathbf{W}(\mathbf{S}\mathbf{W})^+$
B2	PWS	$\mathbf{Q}_w^{-1}\,\mathbf{W}(\mathbf{S}\mathbf{W})^+$
B3	WPI	$\mathbf{W}(\mathbf{S}\mathbf{W}\mathbf{Q}_w)^+$
B4	WMNM	$\mathbf{Q}_w\mathbf{W}(\mathbf{S}\mathbf{W}\mathbf{Q}_w)^+$
C5	WMNM	$\mathbf{Q}_t\mathbf{W}(\mathbf{S}\mathbf{W}\mathbf{Q}_t)^+$

with relative radii (r_a /r_d) of 0, 0.2, 0.4, 0.6 and 0.8 from the origin. For hemiarray cases, the anomaly position was varied in angles (θ) from 0° to 180° with 5° increment. In full array cases, only $\theta = -90°$ was used. The model background conductivity was set to 1, and anomalies represented a unit conductivity increase from the background.

2.15. Phantom experiments

A cylindrical phantom ($r_P = 14.0$ cm) was filled with saline solution (5 L). Vertical bar electrodes (width 13.0 mm and length 101.5 mm) were attached equidistantly around the phantom boundary to create an approximately two-dimensional field pattern. An insulating plastic rod of radius 1.4 cm ($0.1 \times r_P$) was used as an anomaly, and it was moved along the α, $-\beta$ and γ axes (at $\theta = 0°$, $-90°$ and 180°), with the anomaly center placed successively at relative radial displacements (r_A/r_P) of 0 (center), 0.25, 0.5 and 0.75, ten locations in total. This procedure was repeated for different volumes (50, 100, 150, 200 and 250 mL) of anomaly having conductivity similar to that of blood (0.67 S m^{-1}) placed in the background of saline with a conductivity of 0.2 S m^{-1}. We used the ePack eight-channel EIT system (Tang *et al* 2006) to collect measurements. The device was operated at a 2 mA constant current and 62.5 kHz.

3. Results

Results of methods using (15)–(18) were compared in terms of spatial variability. For convenience, each normalization method was given an index as in table 2.

Normalization method C5 defined in the last row of table 2 is based on WMNM reconstruction and WMNM normalization as for B4. However, the normalization matrix $\mathbf{Q}_t$ was used instead of $\mathbf{Q}_w$.

The pseudo-inverted part of the reconstruction matrix can be understood as pseudo-inversion of a matrix product of the normalization matrix ($\mathbf{Q}_t$ or $\mathbf{Q}_w$) and the sensitivity matrix ($\mathbf{S}$). Changes of the system matrix condition number owing to this matrix multiplication are presented in table 3. Table 3 shows that matrix conditions can improve depending on the choice of the normalization matrix. For a full array, $\mathbf{W}$ tended to decrease the condition number, while $\mathbf{Q}_t$ and $\mathbf{Q}_w$ did not. For the hemiarray, $\mathbf{Q}_t$ tended to decrease the condition number, while $\mathbf{W}$ and $\mathbf{Q}_w$ tended to increase them. Therefore, when noisy measurements are

Table 3. Condition numbers of the normalized system matrices

System matrix	Condition number (full array)	Condition number (hemiarray)
S	2.21×10^{17}	2.02×10^{18}
SW	2.00×10^{17}	3.21×10^{18}
$\mathbf{SQ}_t$	6.37×10^{17}	3.93×10^{17}
$\mathbf{SWQ}_w$	2.31×10^{17}	2.51×10^{18}
$\mathbf{SWQ}_t$	2.05×10^{17}	4.10×10^{17}

to be reconstructed, using a normalization matrix that decreases the condition number could be beneficial.

3.1. Ideal measurement reconstructions

Ideal measurements were obtained by individually perturbing all elements by unit conductivity increase. They are effectively columns of the sensitivity matrix. Their corresponding QI values were calculated using (8) for all the measurements. We compared normalization methods in terms of relative STD (RSD: absolute value of variation expressed as standard deviation divided by the average) calculated using all QI values (19):

$$\mathrm{RSD}(\mathrm{QI}) = \mathrm{STD}(\mathrm{QI})/\mathrm{average}(\mathrm{QI}). \tag{19}$$

According to the results in table 4, method A3 resulted in an RSD decrease in all cases, while C5 resulted in an overall decrease of RSD except along the hemiarray α axis.

3.2. Simulated measurement

Simulated measurements were created from the computer models described as in section 2.15. We investigated relative QI (δQI) (9) with the central anomaly as the reference. Maximum deviation errors (ε) away from the central QI value (QI_0) were calculated as in (20) and displayed in table 5:

$$\varepsilon = \mathrm{Max}\{|\delta\mathrm{QI} - 1|\}. \tag{20}$$

Method A3, which was shown to perform most stably in the case of ideal measurements, also reduced ε for simulated measurements. However, it failed to decrease ε for the hemiarray β axis. B4 showed overall decrease of ε for hemiarray cases, but its ε increased for the full array case. C5 produced results similar to the ideal measurement case. Its ε decreased in all cases except for the hemiarray α axis.

3.3. Phantom measurement

Phantom measurements were made as described in section 2.15. The investigation was executed in the same way as in section 3.2. In table 6, ε values are displayed for various volumes of the blood-like anomaly. The ε values were calculated from δQI values calculated from ten different anomaly positions.

Our results in table 6 show that method A2 worked better for anomalies of larger volumes in the hemiarray case. B4 showed a decrease for the hemiarray case, and ε values tended to increase as the anomaly volume increased. This may have been due to our assumption of

Table 4. RSD of QI (19) calculated from the ideal measurement reconstructions (at full rank, $k = 20$) of eight electrode cases

Normalization method	Full array ($\theta = 0°$)	Hemiarray (α: $\theta = 0°$)	Hemiarray (β: $\theta = 90°$)	Hemiarray (γ: $\theta = 180°$)
A1	0.1478	0.1749	0.1734	0.9579
A2	0.3294	0.4000	0.2586	0.4829
A3	0.0628	0.1023	0.1019	0.9095
A4	0.0878	0.1053	0.1790	0.9846
B1	0.1124	0.5440	0.8739	0.1946
B2	1.1087	5.8956	2.9424	16.7774
B3	2.4142	0.8479	0.2373	0.5036
B4	0.2141	0.2729	0.0936	0.8172
C5	0.0672	0.3413	0.0184	0.6702

Table 5. Maximum deviation error (ε) of the relative QI, calculated from the simulated measurement reconstructions ($k = 16$) of eight electrode cases. Truncation number k was chosen based on the l-curve investigation

Normalization method	Full array ($\theta = 0°$)	Hemiarray (α: $\theta = 0°$)	Hemiarray (β: $\theta = 90°$)	Hemiarray (γ: $\theta = 180°$)
A1	0.7239	0.3134	0.7409	0.9539
A2	2.7983	2.2928	0.5365	0.5759
A3	0.2437	0.0671	0.8284	0.9075
A4	0.4398	0.3078	0.8478	0.9574
B1	0.2740	3.9886	2.8486	0.7287
B2	1.0667	4.9794	5.2909	2.2658
B3	0.3379	6.2294	2.2075	0.9253
B4	0.9985	0.1382	0.5224	0.8945
C5	0.2239	0.5944	0.6117	0.7948

reconstructions being the weighted sum of system's PSFs. Method C5 decreased ε values for anomalies of all volumes in both full array and hemiarray cases.

Cross-examination of tables 3–6 allows us make some findings. For the full array, the spatial variability (in terms of relative STD of QI or ε) decreased for A3, A4, B1 and C5. A3 and C5 seem to be the best candidates since they resulted in the most decrease in most cases.

In figure 2 (left), methods A3 and A4, which successfully reduced spatial variability of QI, resulted in blurred reconstruction of a central anomaly compared to reconstructions using B1 and C5, which produced more compact central anomaly. It should be noted that B1 and C5 are methods that are based on WNMN regularization. Method B1 blurred images of the anomaly near the boundary. C5 did not produce a blurred reconstruction of this location. Thus, C5 appears to be the most reasonable method for the full array. In figure 2 (right), selected methods (A1, B1 and C5) were compared in terms of resolution and position error. In order to estimate resolution, we followed definition of the blur radius suggested by Adler and Guardo (1996). Elements that have values greater than half the maximum element value were chosen as the half amplitude (HA) set. Then, the resolution was calculated as a square root of the ratio between the area of the HA set (A_{HA}) and the domain area (A_o) (21):

$$\text{resolution} = \sqrt{\frac{A_{\mathrm{HA}}}{A_o}}. \tag{21}$$

Table 6. Maximum deviation error of the relative QI (ε) calculated from phantom reconstructions of eight-electrode full array and hemiarray topologies. In the full array, the anomaly was placed on four different locations on the negative β axis with relative displacement from the domain center ($r_A/r_P = 0$, 0.25, 0.5 and 0.75). In the hemiarray, the anomaly was placed on ten different locations on the α, $-\beta$, and γ axes ($r_A/r_P = 0$, 0.25, 0.5 and 0.75). Truncation number k was chosen by investigation of the l-curve

	Full array				
	Anomaly volume				
Normalization method	50 mL ($k = 16$)	100 mL ($k = 17$)	150 mL ($k = 17$)	200 mL ($k = 17$)	250 mL ($k = 17$)
A1	0.3344	0.3799	0.3048	0.2631	0.2377
A2	0.8131	0.8741	0.6714	0.6055	0.5685
A3	0.1570	0.1634	0.1517	0.1173	0.1017
A4	0.2266	0.2588	0.2129	0.1760	0.1562
B1	0.1896	0.1918	0.1831	0.1492	0.1318
B2	1.6966	9.6980	17.6351	5.3715	3.5571
B3	0.1961	0.3818	0.1346	0.1869	0.1777
B4	0.4055	0.4456	0.3568	0.3126	0.2852
C5	0.1513	0.1582	0.1483	0.1138	0.0980
	Hemiarray				
	Anomaly volume				
Normalization method	50 mL ($k = 15$)	100 mL ($k = 16$)	150 mL ($k = 16$)	200 mL ($k = 16$)	250 mL ($k = 17$)
A1	0.5084	0.6845	0.4759	0.4213	0.4219
A2	0.5319	0.2658	0.1438	0.2028	0.2872
A3	0.6003	0.6216	0.5373	0.5155	0.5536
A4	0.5923	0.7090	0.5181	0.4819	0.4940
B1	0.6883	0.4502	0.2519	0.4558	0.3855
B2	3.0771	4.5643	8.2285	6.4299	1.3628
B3	0.7296	0.8014	0.7127	0.8695	0.9601
B4	0.4587	0.4695	0.3345	0.3314	0.4013
C5	0.3072	0.2578	0.2660	0.2253	0.2609

The position of an anomaly was located as the center of mass of the HA set in reconstruction images (22):

$$\text{position} = \frac{\sum_m \sigma_m \cdot p_m}{\sum_m \sigma_m}. \tag{22}$$

Here, p_m is the position vector (x_m, y_m) within the domain.

Small and uniform resolution values are regarded to be desirable indicating less blurring. In figure 2, there are overall enhancement of resolution when using B1 and C5. In terms of position error, C5 shows great improvement except when the anomaly was close to the domain boundary.

For the hemiarray case, normalization could be made particularly effective for anomalies on the γ axis. However, this was obtained at the expense of increasing variability along the α axis. Even though B4 and C5 were most effective for β and γ axes anomalies, they were not effective for α axis anomalies (tables 4 and 5). Investigation for various anomaly volumes (50, 100, 150, 200 and 250 mL) used in our phantom experiments (table 6) revealed that B4 and C5 consistently reduced spatial variability. In figure 3, methods that reduced variability

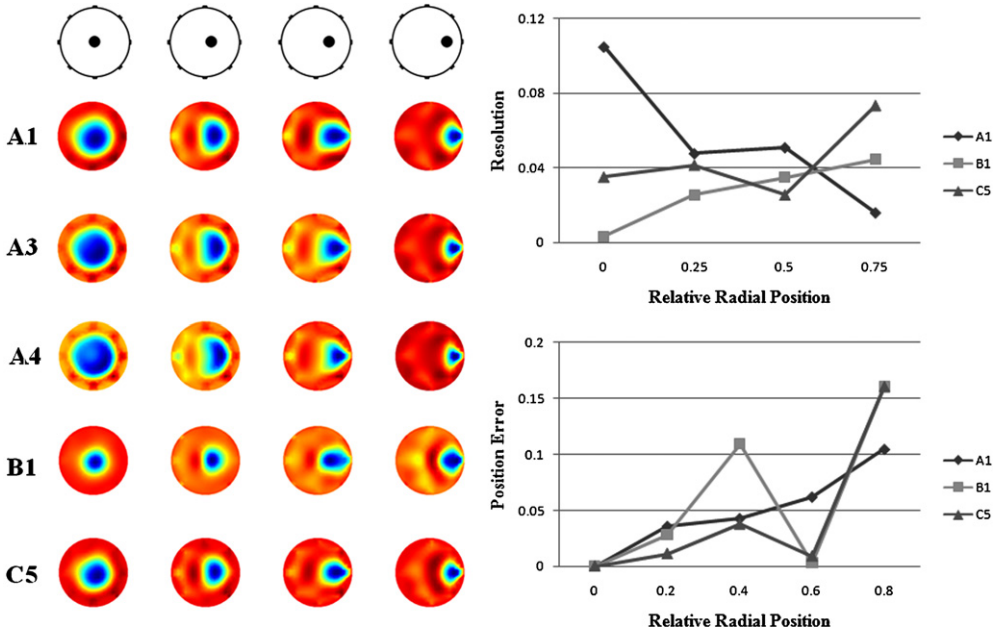

Figure 2. Eight-electrode full array images ($k = 17$) reconstructed from phantom measurements made for a blood-like anomaly (100 mL) in four different locations on the negative β axis ($r_A/r_P = 0$, 0.25, 0.5 and 0.75). (Left) Images reconstructed using normalization methods A1, A3, A4, B1 and C5 are compared. (Right) Images reconstructed using A1, B1 and C5 were investigated in terms of the anomaly's blur radius (resolution) and position error. Resolution was calculated as a square root of the ratio between area of the half amplitude set and the actual anomaly size. Position was estimated as a center of mass of the half amplitude set.

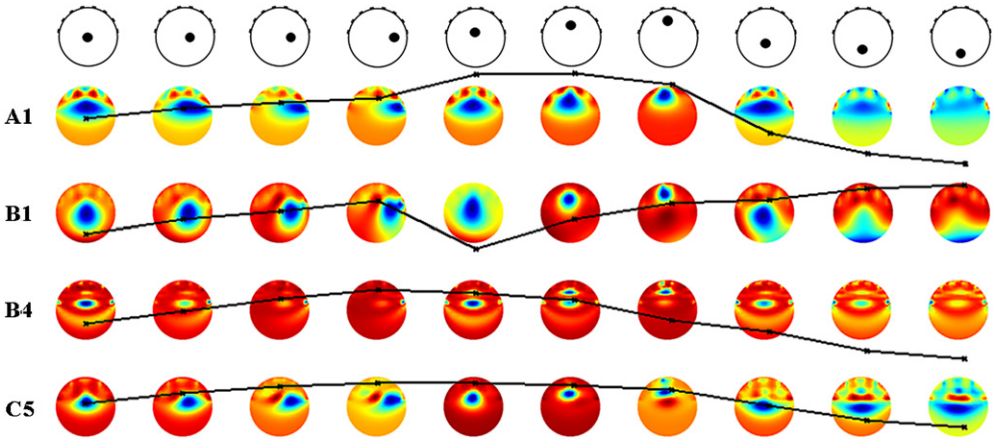

Figure 3. Eight-electrode hemiarray images ($k = 16$) and relative QI curves reconstructed from a blood-like anomaly (100 mL) using methods A1, B1, B4 and C5. Relative QI values were calculated with the central anomaly ($r_A/r_P = 0$) as a reference and scaled to a value of 1. All relative QI plots have the same scale (0.5–2) and have been overlaid on top of corresponding reconstruction images. The anomalies were positioned at ten different locations on the β, α and γ axes ($r_A/r_P = 0.25$, 0.5 and 0.75).

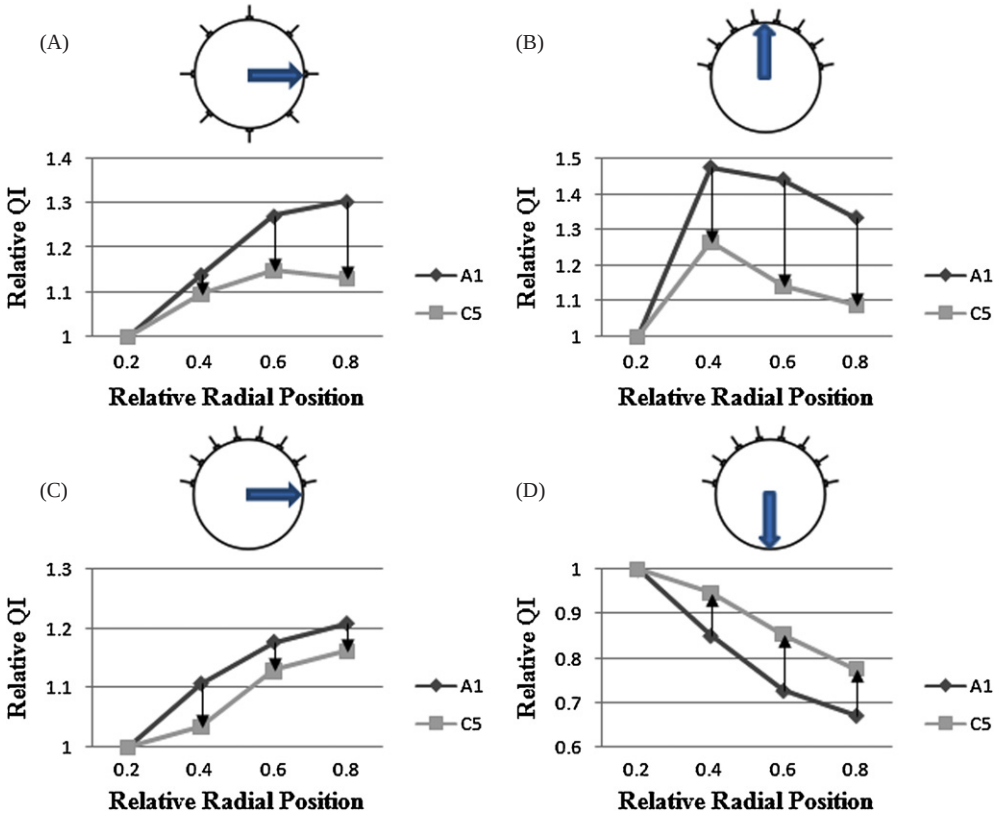

Figure 4. Radial curves of relative QI calculated using TSVD (A1) and normalization method (C5). The QI values are obtained from reconstructions for the full array ($k = 17$) and hemiarray ($k = 16$). The anomaly (100 mL) was positioned on various locations. The curves were plotted for the (A) full array $-\beta$, (B) hemiarray α, (C) hemiarray $-\beta$ and (D) hemiarray γ axes.

are compared for 100 mL anomaly in ten locations. Anomaly images reconstructed using B1 were comparatively less blurry than A1, B4 and C5. In reconstruction of anomalies on the γ axis, B1 reduced the spatial variability. B4 performed well in terms of reducing spatial variability of QI but did not produce a good image quality, as shown in figure 3 (B4). C5 resulted in reduced variability producing images of improved qualities. However, images of anomalies on the γ axis were still unclear.

In figure 4, performance of our proposed method C5 was demonstrated for normalizing QI in the full array and hemiarray topology. The relative QI values were plotted versus the radial axis. The uniformity of the relative QI curves increased, when C5 was used. The improvement was consistent for all axes considered (α, β and γ).

4. Discussion

Image reconstruction in EIT is a nonlinear and ill-posed inverse problem. Uncertainties caused by these properties prevent EIT images from having the high resolution typically found in MRI and CT imaging. However, one may extract a unique property (electric conductivity) of an imaged object in EIT, which is potentially valuable in clinical monitoring. EIT image

reconstruction is a spatially variant estimation problem. In this paper, we attempted to reduce spatial variance of QI. Spatial variance is hard to deal with because its properties also depend on the regularization method chosen. Therefore, we sought a general approach that can reduce spatial variance in this paper. We proposed methods that normalize full array and hemiarray EIT reconstructions using blurring properties calculated directly from the sensitivity matrix as a normalization term. This term is dimensionless, and units of reconstructed quantities were preserved after normalization. We found that the spatial variability observed was dependent on the regularization scheme rather than the inverse model. Additionally, we found that patterns of the spatial variability were similar for different forward models. We chose the model that had elements of similar areas in order to simplify QI calculations.

We implemented normalization of spatially variant EIT image reconstruction using three different methods: PWS, WPI and WMNM. We found in our comparison that PWS methods generally worked poorly in reducing spatial variance. Employing WPI methods (A3 and A4) worked well for the full array but not for the hemiarray. The WMNM-regularized reconstruction (B1) produced images of improved contrast in both full array and hemiarray cases. While B1 succeeded in reducing spatial variability for the full array, it did not reduce variability for hemiarray cases. By using the WMNM framework, but with a differently defined normalization matrix as in C5 ($\mathbf{WQ}_t$) rather than B1 ($\mathbf{W}$), Sadleir *et al* (2008) succeeded in decreasing spatial variability of QI. C5 also produced images that were generally superior to those produced using A1. In our investigation, we confirmed the results of Sadleir *et al* (2008) in terms of QI. Further, we demonstrated that C5 performed fairly well for the full array as well. The images in figure 3 (C5) were reconstructed from phantom measurements, while the images shown in Sadleir *et al* (2008) were reconstructed from noiseless simulated measurements. Our images did not match the images in Sadleir *et al* (2008) closely for anomalies in the γ axis. Even though the condition number of the system matrix of B1 ($\mathbf{SW}$) was larger than that of C5 ($\mathbf{SWQ}_t$) (table 3), anomaly images reconstructed by B1 appeared less diffuse than those by C5 over all regions including the γ axis.

We tested our methods for single anomalies located at various positions within the domain. We have yet to determine if our method works well for multiple anomaly cases. Our normalization scheme was based on 2D and we obtained the blurring matrix from the sensitivity matrix of a 2D inverse model. We applied the 2D normalization method successfully to cylindrical phantom data acquired using bar electrodes. The blur matrix can easily be obtained from a 3D sensitivity matrix, and there is restriction on implementing our normalization method in 3D.

Overall, we found that the best normalized QI values were obtained by applying a WMNM normalization method to WMNM regularization (C5) for both full array and hemiarray topologies. Our comparison showed that C5 was generally superior to other methods, even though there were test cases where it did not perform better than other candidates.

5. Conclusion

In this paper, we compared various normalization methods in terms of QI. We demonstrated that some of these methods successfully reduced spatial variability of QI for the measurements obtained in numerical simulations and phantom experiments. Our investigation included many different approaches to resolve a spatial variability problem in EIT image reconstruction. Although method C5 generally performed well, there was no single method that performed significantly better over both electrode topologies. However, we have showed that discrete

use of this type of normalization method should result in increased quantitation stability in EIT reconstruction.

Further testing of these methods is necessary for more realistic geometries in 2D and 3D. Formulated in a straightforward manner, the methods should be simple to implement without great computational burden. Thus, they should be easily applicable to various image reconstruction problems that are spatially variant. We anticipate that this type of normalization method could also be used for highly asymmetric image reconstruction problems.

Acknowledgments

This work was supported in part by NIH grant RO1EB-002389 and by the US Army Medical Research and Materiel Command under award no W81XWH-07-1-0591, both to RJS.

References

Adler A, Amyot R, Guardo R, Bates J H T and Berthiaume Y 1997 Monitoring changes in lung air and liquid volumes with electrical impedance tomography *J. Appl. Physiol.* **83** 1762–7

Adler A and Guardo R 1996 Electrical impedance tomography: regularized imaging and contrast detection *IEEE Trans. Med. Imaging* **15** 170–9

Barber D C 1990 Quantification of impedance imaging *Clin. Phys. Physiol. Meas.* **11** A45–56

Barber D C and Brown B H 1984 Applied potential tomography *J. Phys. E: Sci. Instrum.* **17** 723–33

Blott B H, Cox S J, Daniell G J, Caton M J and Nicole D A 2000 High fidelity imaging and high performance computing in nonlinear EIT *Physiol. Meas.* **21** 7–13

Clay M T and Ferree T C 2002 Weighted regularization in electrical impedance tomography with applications to acute cerebral stroke *IEEE Trans. Med. Imaging* **21** 629–37

Cohen-Bacrie C, Goussard Y and Guardo R 1997 Regularized reconstruction in electrical impedance tomography using a variance uniformization constraint *IEEE Trans. Med. Imaging* **16** 562–71

Golub G H and Reinsch C 1970 Handbook series linear algebra: singular value decomposition and least squares solutions *Numer. Math.* **14** 403–20

Hansen P C 1987 The truncated SVD as a method for regularization *BIT* **27** 543–53

Hansen P C 1992 Analysis of discrete ill-posed problems by means of the *L*-curve *SIAM Rev.* **34** 561–80

Lionheart W R B 2004 EIT reconstruction algorithms: pitfalls, challenges and recent developments *Physiol. Meas.* **25** 125–42

Malmivuo J and Plonsey R 1995 *Bioelectromagnetism: Principles and Applications of Bioelectric and Biomagnetic Fields* (New York: Oxford University Press)

Meeson S, Killingback L T and Blott B H 1995 The dependence of EIT images on the assumed initial conductivity distribution: a study of pelvic imaging *Phys. Med. Biol.* **40** 643–57

Oh S and Sadleir R J 2007 Compensating spatial variability of quantity index in 2D electrical impedance tomography: Comsol Multiphysics study *COMSOL Conf. (Boston, MA)*

Sadleir R J and Fox R A 1998 Quantification of blood volume by electrical impedance tomography using a tissue-equivalent phantom *Physiol. Meas.* **19** 501–16

Sadleir R J, Zhang S U, Tucker A S and Oh S 2008 Imaging and quantification of anomaly volume using an eight electrode 'hemiarray' EIT reconstruction method *Physiol. Meas.* **29** 913–27

Tang T, Zhang S U and Sadleir R J 2006 A portable 8-electrode EIT measurement system *Proc. 7th Conf. on Biomedical Applications of EIT* pp 190–3

Thomas D C, Siddall-Allum J N, Sutherland I A and Beard R W 1994 Correction of the non-uniform spatial sensitivity of electrical impedance tomography images *Physiol. Meas.* **15** A147–52

Use of an eight-electrode hemiarray EIT electrode configuration for in-vivo fluid quantification

R.J. Sadleir, A. S. Tucker, Sungho Oh and Te Tang

J. Crayton Pruitt Family Department of Biomedical Engineering, University of Florida

Abstract: We applied a novel electrode topology, the 'hemiarray' in conjunction with an eight-electrode EIT system, to detect and quantify fluid administered to the stomach. We also assessed the system in terms of its ability to detect fluid in the presence of normal artifacts such as breathing and motion. We found that our system could easily detect 250 ml of blood-equivalent fluid and displayed relatively low amplitude normal breathing-related artifacts. We found that our new system's performance compared well with an earlier, 16-electrode full array prototype.

Introduction

Electrical Impedance Tomography (EIT) has strengths in its sensitivity and ability to detect real-time changes in body composition due to processes such as bleeding, breathing and gastric emptying (Sadleir 2001, Adler 1997, Nour 1995). The EIT inverse problem is ill-posed and sensitive to noise, and does not provide images of a near-anatomic quality like MRI or CT. However, time series of EIT data are easily obtained, and contain valuable functional information.

Intra-abdominal bleeding is a common consequence of motor vehicle trauma, falls and detonations. In younger patients (under 30) the presence of intra-abdominal bleeding may not be reflected in clinical signs such as blood pressure or pulse rate. If it can be measured, time series data providing both the total amount of abdominal bleeding and bleeding rate are useful indicators to warn both of impending hypovolemic shock, and the urgency of surgery to repair injuries. Bleeding rate data may be used to prioritize patients for surgery in battlefield or mass-casualty situations.

Imaging modalities such as X-Ray, CT, MRI and ultrasound are able to image blood, but are either invasive (X-Ray, CT), difficult to use at the bedside (MRI, CT) or require trained operation and interpretation (ultrasound).

Blood has a large low-frequency conductivity contrast (approximately 3:1) with most abdominal tissue. Therefore, it should be possible to image blood anomalies using EIT. Because EIT can be used in monitoring mode it should also be possible to measure the bleeding rate by analyzing a series of EIT images. Subjects undergoing Continuous Ambulatory Peritoneal Dialysis are ideal models for studying intra-abdominal bleeding as they regularly (4-hourly) administer a conductive fluid (principally saline) to their abdomen. The rate of fluid administration can be measured and correlated with EIT measurements.

We used a 16-electrode EIT prototype system [2, 4] and an inflatable belt that applied electrodes at equidistant spacings about the abdomen [3] and studied properties of reconstructed EIT image sequences collected during peritoneal dialysis fluid exchange. We found that excluding effects of unavoidable artifacts such as bleeding, we were able to see small amounts (ca. 20 ml) of fluid in the abdomen. Including the effects of breathing, we estimated that the system was able to detect 60-90 ml of fluid unambiguously.

A typical EIT 'full array' involves applying electrodes evenly about the plane of interest. However, in emergency medical circumstances this approach is not possible because of the need to avoid lifting patients in circumstances where they may have suffered spinal injury. We developed a novel electrode topology, the 'hemiarray', which only involves application of eight electrodes to the anterior abdominal surface. Although the sensitivity and specificity of such a system would be expected to be much worse because of using fewer electrodes (8 rather than 16) and confining them to only half the plane, we found in a recent phantom study that this system, in combination with new reconstruction algorithm, had a similar sensitivity to the earlier system, which used a linearized backprojection algorithm [1]. We performed these measurements as a prologue to a study repeating the protocol described in [2] using the hemiarray topology and a new system devised for emergency medicine environments [7].

Methods

We used the EPack system [7] in conjunction with an array of eight 1.5" x 6" disposable carbon rubber electrodes (Soft-Touch Platinum SP1540 Ultima Products Limited, Philadelphia, PA). The subject's abdominal girth was measured and the electrodes were placed equidistantly on the anterior abdominal surface such that the distance from the outer edge of the first electrode to the outer edge of the last electrode was half the girth. The subject was asked to lie supine for the duration of the study.

Data was collected at rates between 0.2 and 1 Hz. Subjects were asked to breathe normally, without talking, for the first ten minutes of the study. After this period talking was permitted and after about fifteen minutes' monitoring the subject was asked to breathe with extreme movement of the abdomen (abdominal breathing). After this point the subject resumed normal breathing, and at the thirty minute mark the subject was fed a meal consisting of a conductive fluid (chicken bouillon, 1 cube/250 ml) as two aliquots of 125 ml. A short gap was allowed in between administration of the two samples. After administration the subject was asked to breathe normally until the end of monitoring (10-30 minutes after administration of the meal).

Differential voltage data were processed to images using a two dimensional sensitivity matrix calculated for the hemiarray layout using the weighted minimum norm method described in [1] and [7] . Each image was processed to a single number (the quantity index or QI) representing the amount of conductive fluid in the abdomen as

$$QI = \sum_{p=1}^{TP} \Delta\sigma_p A_p \qquad (1)$$

where $\Delta\sigma_p$ and A_p are the conductivity change observed in pixel p and the area of pixel p respectively. TP is the total number of pixels. QI plots against time were plotted and the relationship between volume and QI compared with phantom data [1].

Results

Figure 1 shows plots of QI against volume observed using the hemiarray system for reconstructions of blood-equivalent anomalies in a large cylindrical phantom. The phantom had electrodes with similar dimensions to the ones used in this study. The graph show QI averages, standard deviations and linear fits over a set of data gathered from anomalies placed at various locations in planes that were respectively in the center of the electrode plane (PL1), one half electrode length away from the electrode center (PL2) and one electrode length away from the center of the electrode plane (PL3), respectively. The mean sensitivity of the system to blood-like anomalies decreased to approximately half when anomalies were moved around at the PL3 level, compared to anomalies moved within PL1.

Figure 2 shows results of one fluid administration and breathing protocol trial in QI terms. Normal breathing and talking was allowed up until about 1000 s, after which abdominal breathing was employed. At about 1300 s abdominal breathing ceased.

Administration of fluid started at about 1700 s.

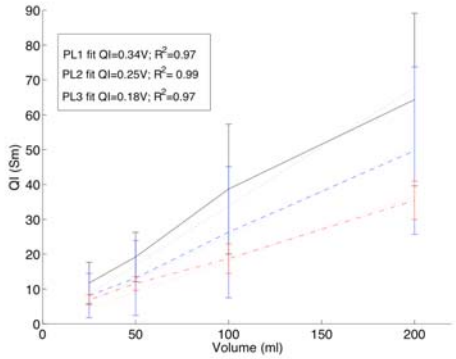

Fig. 1 Plots of QI against volume for hemiarray reconstructions of blood equivalent anomalies of 50, 100, 150 and 200 ml volume in a cylindrical phantom. For each plane, anomalies were placed at relative radial positions of 0 (center) and 0.3 and 0.6 from the center in each of three directions (α: towards the electrode set; β: towards the side of the electrode array; γ: away from electrode set), making a total of 7 positions per plane. Curves show average QI values and linear fits (dotted lines) to data for anomalies moved in (solid line) PL1, (dashed) PL2 and (dash-dot) PL3. Error bars show uncertainties in mean QI estimate considered over all anomaly locations. The maximum volume uncertainty in PL1 was about 40 ml, in PL2 about 70 ml, and in PL3 about 30 ml.

Data from Figure 2 were also processed using the same reconstruction scale used in Figure 1 (Data in Fig. 1 were multiplied by a weighting matrix, whereas Fig. 2 data have not had this scaling applied). The maximal deflection of QI during fluid administration on this scale was about 42/250 ml of fluid, similar to the deflection expected for anomalies appearing in PL3 (QI = 0.18 V, where V is the volume measured in ml). The reduction of sensitivity by half in moving from PL1 to PL3 was also observed in the study of [4]. Further, finding this sensitivity during fluid ingestion is consistent with results observed during a similar fluid ingestion trial performed during the course of experiments described in [2]. The extreme abdominal breathing shows about twice the final amplitude of the administered fluid, being equivalent to an approximately 350 ml anomaly present in PL1. The deviation of QI

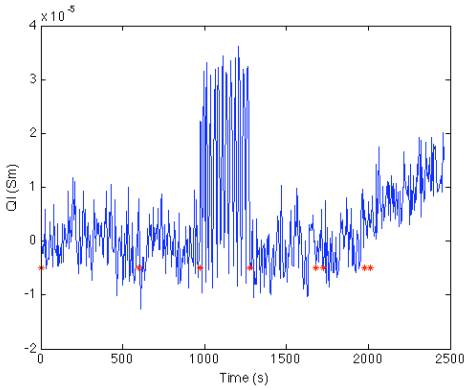

Fig. 2. Quantity indices measured from image sequence (493 samples) showing effects of extreme breathing (central peak). QI values are shown on a different scale to those in Figure 1. Stars on the image indicate, in sequence: the start of the trial, subject being allowed to talk, start and end of abdominal breathing and (closely separated pairs of stars) starting and finishing the first and second soup meals.

measurements during abdominal breathing was found to be strongly positive, representing an apparent increase in conductivity from the reference. Examination of raw differential voltage change data shows that the largest negative voltage changes (decreases in transimpedance) during this phase were in measurements between the two outermost electrodes. We believe the apparent decrease in conductivity is principally a consequence of shape changes during the abdominal breathing phase. The reference data set was gathered when the eccentricity of the abdomen was large. When measuring data from such a shape, equipotential lines will tend to concentrate (i.e. larger voltage differences will occur) on flatter surfaces, and measurements at regions of greater curvature will be smaller, compared to measurements on a perfectly cylindrical profile. When the shape of the abdomen changes to become more round on inspiration, measurements on formerly flat planes of the abdomen will decrease. Because most of the measurements are made on the anterior surface of the abdomen (measurements are not made around the edges of the elliptic profile), the overall differential voltage vector — and thus QI — should therefore increase on inspiration. We observed that normal breathing represented a

standard deviation of around 45 ml in equivalent fluid volume.

Discussion

The results here show that the method has promise for detection of intra-abdominal fluid in-vivo. We note that breathing involving extreme movements of the abdomen strongly affected our quantity measure. However, normal movement and talking did not produce large deflections in the QI measure. We have estimated [2] that an unambiguous sensitivity to blood of around 30 ml is a useful target for critical care environments. At present deflections due to normal breathing are somewhat above this, being about 50 ml. We found in [1] that we can decrease this uncertainty by augmenting the weighting matrix used in reconstruction. However, we believe that we should be able to further lower this uncertainty using better sampling and deconvolution techniques in electronic hardware.

In this application we are bringing the linear imaging properties of EIT to the fore. Rather than concentrating on perfecting and interpreting images, we are instead concentrating on EIT's overall linearity and using an index derived from images as our primary measure. However, images are still of critical importance to our application. If we were to use a four-electrode method (a 'one pixel' method) we would not be able to determine the presence of electrode errors and artifacts. Further, we are able to correct for the inherent spatial variance of electrical measurements, and confirm significant QI deflections occurring at any point within the image plane by referring to normalized images [1].

Conclusion

We applied a novel electrode topology and imaging regularization techniques to the problem of imaging fluid in-vivo. We found that an orally administered conductive fluid could be detected with a sensitivity about half that observed when fluid was administered in the electrode plane in-vitro. Breathing involving extreme abdominal movement was observed to have a significant effect on the image quantity measure. However normal breathing only contributed a relatively small amount (close to the system target of 30 ml) to quantity uncertainties. The system performed well compared to an earlier prototype that used 16 electrodes equally spaced about the plane of interest.

Acknowledgements

This work was supported by US Army Medical Research and Materiel Command under Award No. W81XWH-07-1-0591 to RJS.

References

[1] "Imaging and quantification of anomaly volume using an eight electrode 'hemiarray' EIT reconstruction method", R.J. Sadleir, S.U. Zhang, A.S. Tucker and Sungho Oh, accepted for publication in *Physiological Measurement* (2008)

[2] "Detection and quantification of intraperitoneal fluid using electrical impedance tomography" R.J. Sadleir and R.A. Fox, IEEE-Trans. Biomed. Eng. **48**, 484-491 (2001)

[3] "Inflatable belt for the application of electrode arrays", R.J. Sadleir, R.A. Fox and V.F. Turner, Rev. Sci. Inst. **71**, 530-535 (2000)

[4] "Quantification of blood volume by Electrical Impedance Tomography using a tissue equivalent phantom", R.J. Sadleir, R.A. Fox, Physiol. Meas. **19,** 501-516 (1998)

[5] "Monitoring changes in lung air and liquid volumes with electrical impedance tomography", A. Adler, R. Amyot, R. Guardo, J. H. T. Bates, & Y. Berthiaume, Journal of Applied Physiology **83**, 1762-1767 (1997)

[6] "Applied potential tomography in the measurement of gastric emptying in infants", S. Nour, Y. F. Mangnall, J. A. S. Dickson, A. G. Johnson. & R. G. Pearse, Journal of Pediatric Gastroenterology and Nutrition, **20**, 65-72 (1995)

[7] "A portable 8-electrode EIT measurement system" T. Tang, S. U. Zhang and R.J. Sadleir Proceedings 7th Conference on Biomedical Applications of Electrical Impedance Tomography, Seoul, Korea, 27-31 September, 190-193 (2006)

Portable eight-electrode EIT system for detection and quantification of abdominal hemorrhage.

R. J. Sadleir, A. S. Tucker, Sungho Oh and Te Tang
J. Crayton Pruitt Family Department of Biomedical Engineering, University of Florida

We describe a portable EIT system that can identify, quantify and monitor intra-abdominal hemorrhage. The device is optimized for rapidly identifying abdominal hemorrhage as a result of blunt trauma in motor vehicle accidents and battlefield settings. Our modified form of 2D-EIT utilizes a semicircular array of eight electrodes placed around the anterior abdomen of a supine subject. Robustness has been improved through shortened aperture times, lowered power consumption and improved current source stability. The system implements an improved quantity index (QI) algorithm that extracts quantitative information about anomalous masses within the body. The ePack has been tested in-vivo and shows strong sensitivity to accumulations of fluids in the abdomen.

1. Introduction

Electrical impedance tomography (EIT) is an emerging imaging technique that has not yet gained wide clinical acceptance. The limitations of EIT include low image resolution, high signal-to-noise ratio (SNR), bulky electronics, and the difficulty of applying multiple electrodes to the body. Our system addresses these issues with a novel electrode configuration and a novel algorithm that extracts quantitative information from EIT reconstructions.

The ePack is a portable EIT instrument for detection, localization and quantification of intra-abdominal hemorrhage. Conventional methods of detecting and quantifying fluid in the abdomen include enhanced contrast computed tomography and sonography [1, 2]. Our system is a deployable, low cost alternative that is non-invasive and does not require a trained operator.

The ePack architecture is derived from the single-source Sheffield system [3]. That system employed sixteen electrodes placed equidistantly around the thorax. Our system neglects the eight posterior electrodes as shown in Figure 2, and situates the array around the abdomen rather than the thorax. This *hemiarray* configuration allows for rapid diagnosis of a supine, nonambulatory patient but collects an obviously limited information set. This instrument is designed to gather data using this configuration, endeavoring to extract quantitative information without the posterior electrodes.

Figure 1. Photograph of the ePack.

We estimate quantity by calculating the *quantity index (QI)*, which has been shown to be proportional to the actual volume of bloodlike anomalies[4]. Image reconstruction is one step of this algorithm, but we are more interested in the QI figure than the tomogram. Results collected using this approach are discussed separately [5], as are the algorithms used for reconstruction [6]; herein the primary focus is instrumentation.

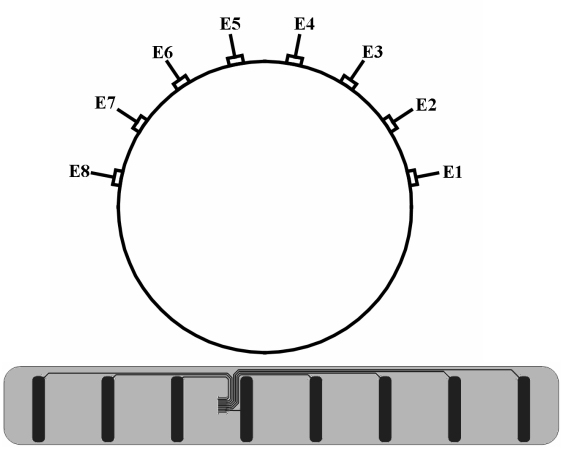

Figure 2. (Top) Overhead view of abdominal cross section showing the *hemiarray* electrode configuration. (Bottom) ePack electrode belt.

2. Methods

The ePack is controlled by a 16-bit DSP (Analog Devices ADSP2181) at 33 MHz. The DSP sends control signals to peripheral hardware, receives measurement data and relays it to the PC control interface. When the ePack is idle, the DSP lowers power consumption by disabling power hungry ICs. The DSP was programmed in C and was compiled using the G21 GCC port.

The constant current supply has three constituents: the waveform generator, voltage to current converter and negative impedance converter. A direct digital synthesizer (DDS) creates the AC voltage waveform. The DDS can output single-tone sinusoids across a wide range of frequencies with variable phase shift (Analog Devices AD9850). We have found it convenient to program the DDS at four frequencies: 15.625kHz, 31.25kHz, 62.5kHz and 125kHz. The DSP controls DDS operation via a 3-wire serial interface.

The voltage-to-current converter is based on a modified Howland topology that accepts a single ended reference waveform from the DDS and converts it into a dual-ended output [7]. The current supply delivers 2mA of peak-to-peak current through the load. Each of the two outputs is connected to an eight-to-one analog multiplexer (Analog Devices ADG408) which distributes the current sink and source to any of the eight electrodes. Multiplexer switching is handled by the DSP.

Sink and source currents are capacitively coupled to the patient. McEwan, Cusick, and Holder have described how this coupling limits the output impedance of the current source [8]. Driven electrode screening lowers the parasitic capacitance in the electrode leads and shields against noise.

The ePack sequentially injects current through each of the eight adjacent electrode pairs. For a given current injection, five adjacent voltage differentials are measured, yielding a total of 40 voltmeter readings in a measurement set.

The voltmeter measures the differential voltage between two arbitrary electrodes. A pair of eight-to-one analog multiplexers (Analog Devices ADG408) selects among the eight electrodes. These inputs are passed to a programmable instrumentation amplifier with 60dB gain (Burr-Brown PGA202). Amplifier output is bandlimited at 200kHz to reduce high frequency interference.

The single-ended output of the gain stage is level-shifted using analog circuitry before it is digitized using a 14 bit ADC (AD9240). The DSP generates the ADC clock signal at 32 times the DDS output frequency, and receives the 14-bit conversion result via DMA. Each voltage reading captures 125 cycles for a total length of N=4000 samples.

The ePack electrode belt connects to the ePack using a ZIF connector, and incorporates shielded traces to lower noise and stray capacitance. We also use commercially available 1.5” x 4” TENS electrodes.

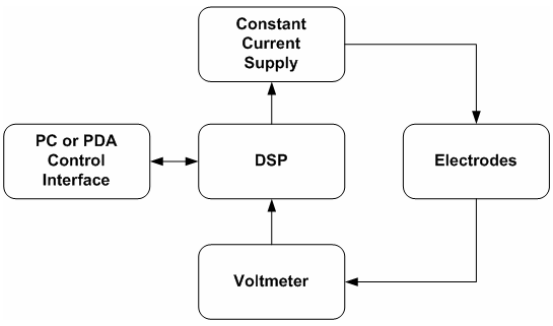

Figure 3. ePack Architectural Diagram.

The PC or handheld PDA user interface controls ePack operation and receives data via RS232 or Bluetooth interface. The user software communicates directly with the ePack: initiating measurements, receiving data and changing internal ePack settings. By optimizing communications between the ePack and the control interface we have been able to maximize data throughput. The control center is written using Visual C# 2005.

External power is applied to the ePack from an isolated transformer or battery packs. Linear regulators condition the external power and deliver it to the ePack's subsystems via three power supplies. The first power supply is a 5V line used for digital ICs including the DSP. A second 5V supply powers low current analog circuitry including the DDS, and A/D converter. A bipolar +/-12V power supply is used for amplifiers, constant current source, and analog switching ICs.

The ePack measures 9"x 9"x 4". On the front panel are the power switch and power indicator. Connections for the external power supply and serial communication are on the rear panel. Eight BNC connectors on the top panel accept input from electrodes.

3. Results and Discussion

Multiplexing introduces parasitic capacitance at the output of the current supply, which lowers the output impedance of the current supply. Some EIT systems inject current using a dedicated current source for each output, eliminating the need for multiplexers [9]. These systems are more flexible due to the abundance of current sources, however they are larger, more expensive, and more difficult to calibrate. Instead, we compensate for stray capacitance using negative impedance converter (NIC) circuitry connected to the sink and source outputs. This method improves the current source output impedance, but still requires calibration. Furthermore, if the output capacitance seen by the current source is variable, the NIC effectiveness is undermined.

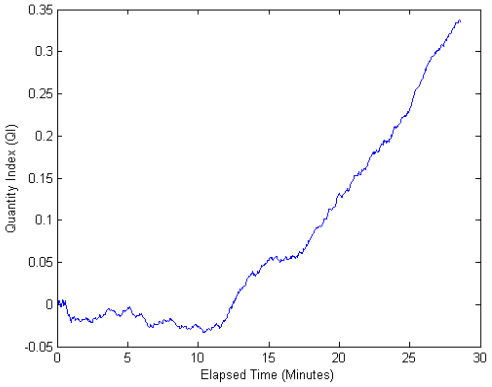

Figure 4. QI plot of a subject drinking and digesting soup. First ten minutes of the curve show resting baseline. At the ten minute mark 250ml soup was consumed.

We define the amount of time necessary to collect a measurement set as the *aperture time*, and the total time required to collect a measurement set, process the data and transmit it to the control interface as the *frame rate*. Using the DSP real-time counter, we measured the aperture time to be 386 ms. Frame rates around 1.5 frame/s are achievable.

Some EIT architectures use multiple voltmeters to increase acquisition speed [10]. In those systems multiple differentials can be measured in parallel rather than in series, however additional calibration is needed to ensure uniformity among the voltmeters. In our system, the multiplexer switching time is on the order of the time required to process the intermediate data from each sampling cycle, therefore multiplexer switching time is not the limiting factor. Other important factors limiting frame rate include the current injection frequency, the number of samples in each voltage reading (N), and the amount of available memory.

We assessed the sensitivity of the ePack in vivo using chicken soup to model blood accumulation in the abdomen. Volunteers fasted for at least twelve hours before the experiment. Then we used the ePack to monitor subjects lying supine. After ten minutes of baseline measurement, subjects consumed 250mL of soup. We expect to see

an increase in QI as the high conductivity fluid accumulates.

Results of soup model show that this instrument is sensitive to changes in abdominal conductivity resulting from ingestion (Figure 4). Fluid does not reach the area of greatest electrode sensitivity until it passes through the stomach. Because the electrode plane was inferior to the stomach, we have observed a ramping measurement rather than a sharp step. The data suggests that this architecture has the capability to detect changes in abdominal impedance.

5. Conclusion

We have designed and tested an EIT system that uses the unique hemiarray electrode configuration. The system is small enough to fit in an ambulance or helicopter and is robust enough to operate despite low SNR. The system shows promise as a practical method for detection of intra-abdominal bleeding, and will benefit from further research in electrode placement, instrumentation and miniaturization.

This work was supported by US Army Medical Research and Materiel Command under Award No. W81XWH-07-1-0591 to RJS.

References

[1] L. N. Nazarian, A. S. Lev-Toaff, C. M. Spettell, and R. J. Wechsler, "CT assessment of abdominal hemorrhage in coagulopathic patients: impact on clinical management." *Abdominal imaging*, vol. 24, no. 3, pp. 246-249, 1999.

[2] M. Blaivas and D. Theodoro, "Intraperitoneal blood missed on a fast examination using portable ultrasound," *The American Journal of Emergency Medicine*, vol. 20, no. 2, pp. 105-107, March 2002.

[3] B. H. Brown and A. D. Seagar, "The sheffield data collection system," *Clinical Physics and Physiological Measurement*, vol. 8, no. 4A, pp. 91-97, 1987.

[4] R. Sadleir and R. Fox, "Quantification of blood volume by electrical impedance tomography using a tissue-equivalent phantom," *Physiological Measurement*, vol. 19, no. 4, pp. 501-516, 1998.

[5] R. J. Sadleir, A. S. Tucker, Sungho Oh and Te Tang, "Use of an eight-electrode hemiarray EIT electrode configuration for in-vivo fluid quantification." *This conference.*

[6] R. J. Sadleir, S. U. Zhang, A. S. Tucker and Sungho Oh, "Imaging and quantification of anomaly volume using an eight electrode 'hemiarray' EIT reconstruction method," Accepted for publication in *Physiological Measurement.*

[7] P. Bertemes-Filho, et al., "Capacitive-compensated current source used in electrical impedance tomography," XII ICEBI V EIT 2004 Gdansk.

[8] A. McEwan, G. Cusick, and D. S. Holder, "A review of errors in multi-frequency EIT instrumentation," *Physiological Measurement*, vol. 28, no. 7, pp. S197-S215, 2007.

[9] Tong In Oh, Eung Je Woo and D. S. Holder. "Multi-frequency EIT system with radially symmetric architecture: KHU Mark1," *Physiological Measurement*, vol. 28, no. 7, pp. S183-S196, 2007.

[10] D. S. Holder. Electrical Impedance Tomography: Methods, History and Applications. Institute of Physics series in medical physics and biomedical engineering, 2005.

Preliminary Results from the E-Pack2: a Portable EIT System Optimized for Detecting Hemoperitoneum

A. S. Tucker, R. J. Sadleir, Tang Te

One potential clinical application of electrical impedance tomography (EIT) is detection of internal bleeding. We are developing an EIT methodology consisting of a unique electrode array and a robust post-processing algorithm that can detect and quantify bleeding in the abdomen. The E-Pack, our first prototype EIT device, was designed to collect data to verify our method. The device was optimized for rapidly identifying abdominal hemorrhage as a result of blunt trauma in motor vehicle accidents and battlefield settings. In this paper we describe and evaluate an improved version of that system, the E-Pack2. Experimental results obtained using resistive and saline-tank phantoms show that the E-Pack2 has significantly improved performance in terms of speed and accuracy compared to its predecessor, despite being half the size. The average signal-to-noise ratio (SNR) in resistive and saline-tank phantoms was 65dB and 39dB, respectively. We have collected data using two *in vivo* models simulating abdominal bleeding. In one model, volunteers drank chicken soup having the same conductivity as free blood. In the second model patients undergoing peritoneal dialysis because of renal failure were monitored during a routine dialysate exchange. In both models, the volume of conductive fluid introduced into the abdomen was measured and compared with the estimate obtained from E-Pack2 data. Preliminary results show improved sensitivity to both ingested and infused conductive fluids, and suggest bleeding rates slower than 100ml/min can be detected. We expect that further improvements to the electrode interface and the reduction of cabling will improve the system's integrity and noise performance.

E-Pack Quick User Guide

E-Pack Control Center Layout

1. **System Status**
2. **Reset Button**
3. **Electrode Quality**
4. **Start/Stop Patient Monitor**
5. **Patient Metrics**
6. **Impedance Image**
7. **Blood Loss History**

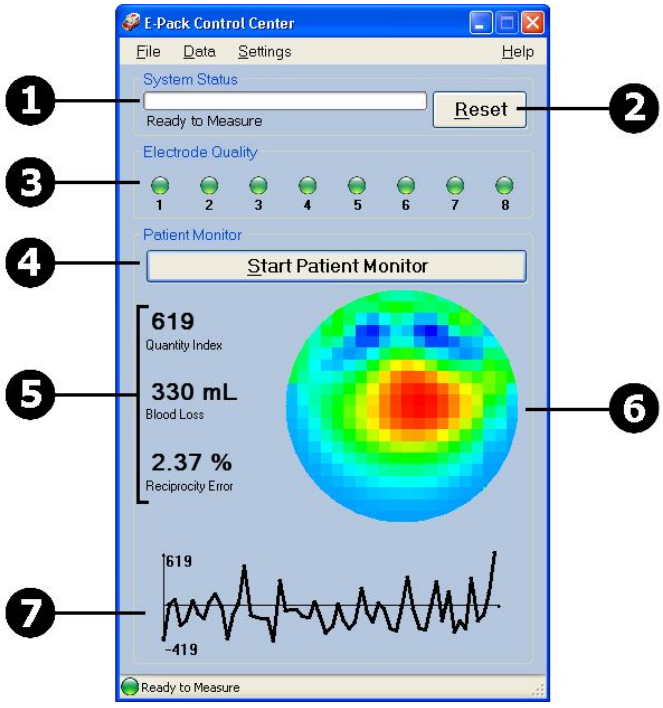

E-Pack Patient Monitor Instructions

1. Start the E-Pack Control Center on the PDA or laptop computer.

2. Turn on the E-Pack using the switch on the front of the unit. The E-Pack Control Center automatically detects the E-Pack when it is powered on.

3. Attach the electrode belt to the patient's anterior abdomen. Proper connection of each of the eight belt electrodes is indicated by green lights in the Electrode Quality window. Red lights indicate that electrodes are not contacting the skin. Adjust the belt until all lights are green before continuing to the next step.

4. Press the Start Patient Monitor button. A prompt appears for the patient identifier. Input the appropriate name or number and press OK. The E-Pack continuously monitors the patient in this mode.

5. When monitoring is no longer necessary, click the Stop Patient Monitor button. Then, turn off the E-Pack using the switch on the front of the unit. Finally, remove the electrode belt from the patient.